A MODULAR PLATFORM FOR INTRUSIVE DIAGNOSTICS AND TPS TESTING IN THE ONR-UTA ARC-JET FACILITY

by

BLAKE HAMILTON

Presented to the Faculty of the Graduate School of

The University of Texas at Arlington in Partial Fulfillment

of the Requirements

for the Degree of

MASTER OF SCIENCE IN AEROSPACE ENGINEERING

THE UNIVERSITY OF TEXAS AT ARLINGTON

DECEMBER 2021

Acknowledgements

I would like to thank my advisor Prof. Luca Maddalena for his guidance and for always pushing me to improve in all aspects of my professional life. I am also thankful to Dr. Davide Viganò for his guidance and suggestions at every step of my work. My colleague Ian Raybon was also a great help, particularly in setting up the motors for the platform. I would also like to thank Dr. Vijay Gopal, Daniel Palmquist, and David Carter for always providing wide-ranging support during my time at the Aerodynamics Research Center.

I would like to thank Scott Eichmann and Rex Winfrey, along with the entire UTA machine shop for their suggestions and excellent fabrication work.

I am thankful for my family for the support they provided, particularly my father Michael L. Hamilton. I would not have been able to complete my work without his help and guidance at every step of my life.

I am also thankful to my classmates and friends Nick Hergenrother and Sandeep James for helping me through all of the late nights of studying during graduate school.

This material is based upon research supported by, or in part by, the U.S. Office of Naval Research under award number N00014-19-1-2250.

December 17, 2021

Abstract

A MODULAR PLATFORM FOR INTRUSIVE DIAGNOSTICS AND TPS TESTING IN THE ONR-UTA ARC-JET FACILITY

Blake Hamilton, M.S.

The University of Texas at Arlington, 2021

Supervising Professor: Luca Maddalena

This work presents an approach to the design, and successful experimental implementation, of a modular platform for intrusive diagnostics and TPS testing in the ONR-UTA Arc-Heated Wind Tunnel "Leste" Facility. The harsh conditions typical of arc-jet facilities (hypersonic, high-enthalpy, chemically-reacting, continuous flows) present a challenge to the design of insertion platforms. In this work a detailed analysis of the aerothermal loads is used to aid in the design process. Specific design points for this modular platform and its ancillary instrumentation have been identified. Based on this design approach, a modular platform for intrusive diagnostics and TPS testing has been developed. This platform features a multi-axis translating carriage and actively-cooled insertion arms for continuous arc-jet operation. It is capable of hosting a variety of intrusive test articles. This platform has been manufactured, integrated, and successfully tested in the ONR-UTA arc-jet "Leste" Facility.

Table of Contents

List of Illustrations

List of Tables

Chapter 1

Introduction

Arc-jet facilities have been widely used to simulate hypersonic flight conditions. These facilities play a fundamental role in the development, testing and evaluation of thermal protection systems (TPS) for hypersonic and space re-entry vehicles. In addition, these facilities can also be used to pursue fundamental flow characterization efforts utilizing traditional intrusive instruments and advanced laser-based diagnostic tools. The flow harshness seen in arc-jet facilities, due to the long duration high enthalpy conditions, present a difficult challenge. In addition, the inherit complexities of a high enthalpy, chemically reacting, non-equilibrium flow, make the prediction of these conditions non-trivial.

One of the primary scopes of arc-jet facilities is the testing and evaluation of TPS materials. The high stagnation enthalpy in hypersonic flows results in very high surface heat flux on vehicles traveling in this regime. In order to protect these vehicles from the high surface heat flux, TPS materials must be developed and qualified. Further, TPS systems serve as a single point of failure on vehicles, adding significance to the qualification of these systems. In order to evaluate TPS systems, arc-jet facilities provide similar levels of surface heat flux and surface shear stress for long durations, allowing proper qualification of these materials for flight conditions.

For long duration exposure, typical of TPS testing, active cooling is required for the model holder to withstand the harsh conditions in the arc-jet plume. Different strategies have been adopted by different facilities. These range from embedded cooling channels to external copper tube wrapping, depending on the specific facility flow conditions. Heat sinks are also used, although these limit the test duration time and are more suited for flow characterization instruments that do not require long exposures to the hot plasma.

An overview of insertion systems in other high-enthalpy facilities is presented in the next section. However, model support systems are not often mentioned or reported in various works, and they do not represent the primary focus of the available literature when they are reported [1–6]. This lack of available literature presents a challenge to the design of insertion systems.

The scope of this work was to design, build, and test a new platform for insertion of instruments and TPS specimens for the ONR-UTA Arc-Heated Wind Tunnel *Leste*. Specifically:

- design, analysis, and manufacturing of two modular liquid-cooled insertion arms capable of mounting instruments for flow characterization and/or performing qualification of TPS material specimens.
- design, analysis, and manufacturing of a carriage assembly which provides two degrees of active motion for the insertion arms and allows for a smooth, fast (to fulfill the requirement for velocity of insertion of null-point calorimeters [on the order of 1 m/s constant speed] as will be specified in the body of the thesis), and accurate positioning of the insertion arms for stagnation point studies.
- conduct experimental test and verification of the entire modular platform thermomechanical characteristics and fulfillment of the design requirements under representative arc-jet flow conditions.
- development of additionally tools and instruments, such as alignment devices and pedestals for multiple insertion arms.

Because of the challenge of designing for high enthalpy, chemically reacting flows, particular focus is given to the aerothermal analysis, thermal management, and response dynamics of the entire system.

1.1 Brief Overview of Model Support Systems

As the performance and architecture of arc-jets vary widely, the design requirements of the insertion system are tailored to the specific facility. These include aerothermal loads, insertion system dynamics, and geometric constraints. In order to prevent test article exposure to the plume during wind tunnel start-up and ramp-up procedures, these facilities typically use insertion systems with at least one axis of active motion. Table 1-1 offers a comparison of selected arc-jet facilities.

Table 1-1 Comparison of Selected Arc-Jet Wind Tunnels

Facility	Arc-Heater Power (MW)	Max Bulk Enthalpy (MJ/kg)	Max Plenum Pressure (bar)	Max Mach Number	Max Mass Flow Rate (kg/s)
UTA-ONR *Leste*	1.6	10	8	6	0.18
NASA Ames IHF	60	28	10	9	1.7
NASA Ames AHF	20	28	40	12	
SCIROCCO PWT [7]	70	45	87	12	3.5
AEDC H1	30	20	100	3.5	3.6
AEDC H2	45	13	12	8.3	4.5
AEDC H3	70	20	115	3.5	11.3

The NASA Ames 20 MW AHF (Aerodynamic Heating Facility) and 60 MW IHF (Interaction Heating Facility) utilize two different article insertion systems [8]. The AHF, used for testing thermal protection systems on interplanetary probes and the space shuttle, typically uses a segmented arc-heater but may also use a Huels-type arc-heater. It uses five separate carriages for test articles, plus one dedicated overhead swing arm containing a heat flux gauge and a pitot tap (Figure 1-1). All five carriages may insert the test article vertically into the plume, or two articles may be inserted laterally into the plume during a single run. The IHF, designed specifically for testing large models simulating shuttle re-entry conditions, uses only a segmented arc heater, and it uses two swing-arm systems on

either side of the nozzle to insert test articles (Figure 1-2). Both systems use arms with similar geometry: an L-shaped tube wrapped in external cooling lines.

Figure 1-1: NASA Ames AHF model support system [8].

Figure 1-2: NASA Ames IHF model support system [2].

The SCIROCCO Plasma Wind Tunnel of the Italian National Aerospace Research Center (CIRA) arc-heated test facility which uses a 70-MW segmented arc-heater to provide up to 45 MJ/kg of bulk enthalpy and flow up to Mach 12 [7]. This facility uses a Model Support System (Figure 1-3) that rotationally inserts the test article and can move the model in both lateral and vertical directions. Additionally, the system allows pitch angles of ±20°, and includes water cooled arms with instrumentation for intrusive diagnostics such as heat flux, pressure, and temperature [9].

Figure 1-3: CIRA SCIROCCO Model Support System [10].

The Arnold Engineering Development Center is a US Air Force facility which operates the H1, H2, and H3 arc-jet wind tunnels. H1 and H3 are segmented arc heaters operating at up to 30 MW and 70 MW respectively. H2 formerly used a Huels-type arc heater, which was upgraded to a segmented arc-heater in 2017 operating at up to 45 MW (Figure 1-4)[11]. The H1 facility utilizes a rotating arm system which holds up to 7 test articles, while H2 facility utilizes a five-arm rotating article insertion system [11].

Figure 1-4: AEDC H2 insertion system [11].

1.2 UTA-ONR "*Leste*" Facility

The newly developed ONR-UTA Arc-Heated Wind Tunnel *Leste* (Figure 1-5) of the Aerodynamics Research Center at the University of Texas at Arlington is equipped with a Thermal Dynamics F-5000 Huels-type arc-heater (power rating 3 MW) powered by a Halmar 1.6 MW DC power supply. Nominal bulk enthalpies range from 1 to 10 MJ/kg at plenum pressures up to 8 atmospheres. The facility is designed to operate with a modular nozzle assembly comprised of a M=2, M=4, and M=6 insert.

The Huels-type arc-heater used in the facility consists of a cylindrical cathode in the upstream end of the device and a cylindrical anode on the downstream end. The electrodes are separated by a boron nitride. A voltage is generated between the electrodes such that an arc is formed in the cavity between the electrodes. The test gas is injected such that it forms a vortex through the barrel of the arc-heater, stabilizing the arc. The arc-

heater allows plenum pressures up to 8 bar, and the walls are water cooled to allow continuous operation.

Downstream of the arc-heater, a water cooled modular conical nozzle assembly expands the gas to the desired Mach number [12]. The nozzle exit is located at the inside wall of a 1.8 m diameter, 2 m length cylindrical stainless steel vacuum chamber which serves as the test section. The test gas then enters a 480 mm diameter catch cone and travels through a diffuser which is designed to slow down the low Reynolds number, high enthalpy flow to subsonic speeds to recover pressure. Between the diffuser and the vacuum pumps is a heat exchanger which removes heat from the test gas to an external water cooling system.

Inside the test section, the facility features a fully water cooled, 2-axis motorized platform to insert and retract test articles from the flow (which is the scope of this work). An array of intrusive instruments have been designed and experimentally validated, these include an in-house developed slug-type calorimeter with ceramic insulation (both Mach 6 and 4 holders are available), pitot probe, and shear wedge platform. Null-point calorimeters and Teflon probes can also be utilized.

Table 1-2 ONR-UTA Arc-Heated Wind Tunnel nominal data

Property	Value
Arc-Heater power	1.6 MW
Bulk enthalpy	1 – 10 MJ/kg
Max plenum pressure	8 atm
Nozzle segments	Mach 2, 4, and 6

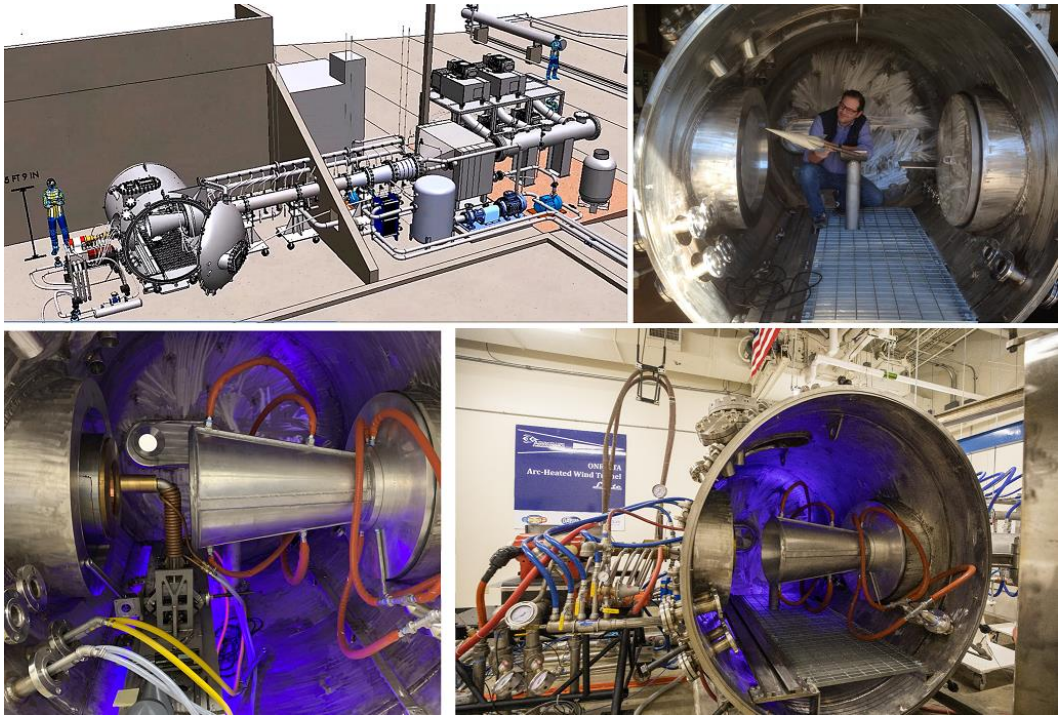

Figure 1-5: ONR-UTA Arc-Heated Wind Tunnel overview.

Additionally, a number of optical ports in the test section can be used for advanced non-intrusive laser-based diagnostics. These techniques include femtosecond Two-photon Absorption Laser Induced Fluorescence (fs-TALIF), Femtosecond Laser Electronic Excitation Tagging (FLEET) velocimetry, and Coherent Anti-stokes Raman Scattering spectroscopy (CARS). fs-TALIF is used to measure chemical composition (atomic Oxygen and Nitrogen), FLEET is used to measure the flow velocity and turbulence intensity, and CARS is used to measure translational and vibrational temperatures. A variety of cameras and pyrometers can also be installed with different viewing angles.

Chapter 2

Design Approach

2.1 Requirements

This section outlines the design requirements that were identified for the modular insertion platform. The hypersonic, high-enthalpy, chemically reacting flow impose significant thermo-mechanical loads on the insertion platform. For this reason, a detailed study was conducted to identify these loads.

Thermal loads are one of the primary drivers in the design of insertion systems for arc-jet flows. Stagnation point heat fluxes in the hypersonic, high enthalpy, flow can quickly heat common construction materials, like copper or steel, beyond their thermo-mechanical limits within a few seconds. Because testing times can be the on order of several minutes, active cooling is required to ensure safe operation of the system and enable rapid turnaround between successive tests.

The system is subject to aerodynamic loads on both the insertion platform arm and the connected test article, where the latter can vary considerably based on the specific application. The attached instrument must remain in its nominal position within a set tolerance as excessive deflection would result in measurements errors. The loads vary depending on the attached instrument; for example, non-symmetric wedges for shear flow measurements present lift and moments in addition to the drag typical of axisymmetric calorimeters. These aerodynamic forces are calculated for a variety of flow conditions and fed into a simplified model of the structure to determine the magnitude of the overall system deflection. The maximum deflection at the test article is ±1mm from the nozzle centerline.

To fully characterize the spatial variation in flow properties the insertion platform must be able to translate in all three dimensions. Movement in two of these dimensions, the vertical and lateral motion with respect to the nozzle exit plane, are motorized.

The platform is inserted into the flow along the lateral direction, and this requires smooth, fast, and accurate motion. The insertion time, defined as the time between the moment that the test article enters the plume and the moment that the test article comes to rest at the nozzle centerline, should be less than or equal to 0.25 seconds. Secondary motions after the halting of the platform may result in poor data collection immediately after the primary motion ends, so the motor must use a controller that can apply a smoothed motion profile, and the mechanism itself must be stiff and with limited play.

The lateral motion mechanism must also provide a constant velocity sweep capability for the use of a null-point calorimeter. Null-point calorimetry are typically swept at a slow enough speed across the plume to allow the sensor to make an accurate measurement, but fast enough to avoid damage to the probe itself [13]. Although the required velocity depends on the time response and geometry of the particular null-point calorimeter which is yet to be designed, one calorimeter design [14] uses a sweep velocity of 1 m/s. So, a constant velocity sweep at 1 m/s is set as a requirement for the insertion platform.

The vertical motion axis, on the other hand, is not the insertion axis so fast motion is not required. Typical vertical motion profiles would be expected to be over small distances while the test article is not in the plume, reducing the urgency of the motion. Nevertheless, the vertical motion axis must be accurate and with limited play in the mechanism. Additionally, the mechanism must be compact and shielded from the immense heat radiated from the shock layer on the arm and test article.

Flow blockage, the ratio of the projected area of the immersed body to the nozzle exit area, is a design constraint which must be considered. Excessive blockage can lead to a reduced efficiency of the hypersonic diffuser and, in more severe cases, in the diffuser unstarting. Therefore, the design must limit the projected exposed frontal area to under 33% of the nozzle exit area.

2.2 Thermal Loads

In this section the thermal loads and their estimation methods are discussed. Particularly, two different approaches are presented for the Mach 4 and 6 arms. Different blockage and thermal constraints (which are detailed below) led to significantly different final designs (as shown in Figure 2-31).

2.2.1 Control Volume Analysis

In order to determine a framework to relate the thermal loads of the system to the cooling performance of the system, a control volume analysis was performed. First, system boundaries must be defined in the form of a control surface. The control surface (Figure 2-1) contains the system entirely within its boundary, while the surroundings lie entirely outside the boundary. For a notional cooling system in the form of a tube with coolant flowing through it, the control surface may be further defined as the inner tube surface and the cross-sectional surfaces perpendicular to the flow axis across the inlet and outlet (Figure 2-2)

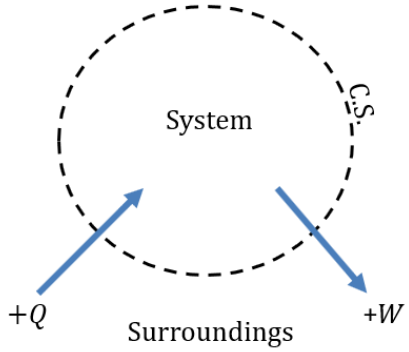

Figure 2-1: Control surface.

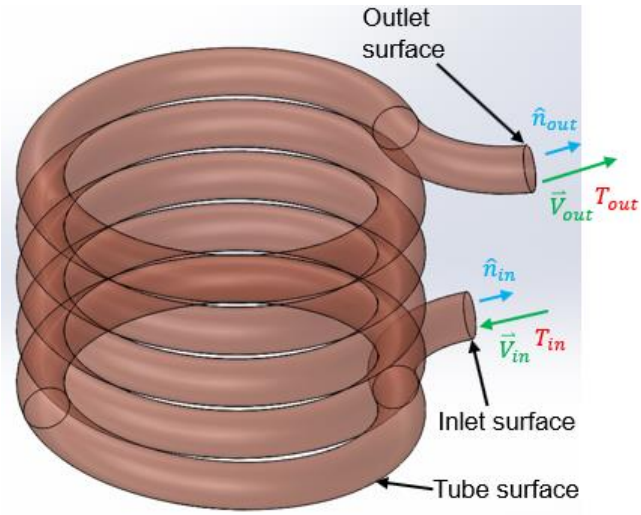

Figure 2-2: Notional schematic of cooling passage surfaces for control volume analysis.

The first law of thermodynamics states that the difference between two equilibrium states of energy of a closed system is equal to the heat transferred from the surroundings to the system across an arbitrary control surface or system boundary (Figure 2-1), or

$$\Delta E = Q - W \qquad (2\text{-}1)$$

where E is the total energy in the system, Q is the heat added to the system from the surroundings, and W is work done by the system on the surroundings.

If the system does not significantly depart from thermochemical equilibrium on a local timescale, then the differential form may be used.

$$\delta E = \delta Q - \delta W \tag{2-2}$$

Then, taking the derivative of (2-2) results in the rate form of the first law of thermodynamics.

$$\frac{dE}{dt} = \dot{Q} - \dot{W} \tag{2-3}$$

The insertion arm cooling system is an open system, because mass is crossing the system boundary. So, Reynold's Transport Theorem is required to continue. Reynold's Transport Theorem states that the rate of change of energy in the system is equal to the rate of change in the energy inside the system plus the rate of energy flowing across the system boundary.

$$\frac{dE}{dt} = \frac{d}{dt}\iiint_V (\rho e)dV + \oiint \rho e(\vec{v} \cdot \hat{n})\, dA = \dot{Q} - \dot{W} \tag{2-4}$$

where ρ is the density of the working fluid, e is specific internal energy, V is volume, A is area, v is velocity, $\hat{n}$ is the surface normal vector, and e is

$$e = u + \frac{\|\vec{v}^2\|}{2} + gz \tag{2-5}$$

Here, u is the specific internal energy, $\frac{\|\vec{v}^2\|}{2}$ is the specific kinetic energy, and gz is the specific potential energy. Since the insertion arm cooling system operates at a steady state condition, the first term in Reynold's Transport Theorem can be neglected, leaving

$$\frac{dE}{dt} = \oiint \rho e(\vec{v} \cdot \hat{n})\, dA = \dot{Q} - \dot{W} \tag{2-6}$$

Work can now be separated into three components: shaft work, pressure work, and viscous work.

$$\dot{W} = \dot{W}_{shaft} + \dot{W}_{pressure} + \dot{W}_{viscous} \tag{2-7}$$

where pressure work, $\dot{W}_{pressure}$, is

$$\dot{W}_{pressure} = \oiint p(\vec{v} \cdot \hat{n})\, dA \tag{2-8}$$

and viscous work, $\dot{W}_{viscous}$, is

$$\dot{W}_{viscous} = \oiint (\vec{\tau} \cdot \vec{v})\, dA \tag{2-9}$$

There is no shaft work, because there is no shaft (or other means of performing shaft work) crossing the boundaries of the control volume. There is, however, pressure work because fluid is moving against a pressure gradient on the inlet and outlet surfaces.

Now, the viscous term is the area integral of the dot product of the shear stress and the velocity along the control surface. On the inlet and outlet, the shear stress term is perpendicular to the velocity vector, so the dot product of shear and velocity is zero and the viscous work at the inlet and outlet is zero. Along the tube inner surface, the velocity is zero due to the no slip condition of fluid flow along a wall.

So, there is zero viscous work along all three of the surfaces, which leaves

$$\dot{W} = \dot{W}_{pressure} \tag{2-10}$$

Combining (2-6) and (2-10) results in

$$\dot{Q} - \dot{W}_{pressure} = \oiint \rho e(\vec{v} \cdot \hat{n})\, dA \tag{2-11}$$

Combining with (8) and consolidating the surface integrals

$$\dot{Q} = \oiint \rho \left(e + \frac{p}{\rho}\right)(\vec{v} \cdot \hat{n})\, dA \tag{2-12}$$

Now, specific enthalpy, h, is defined the sum of specific internal energy and pressure divided by density.

$$h = u + \frac{p}{\rho} \tag{2-13}$$

Combining (2-5), (2-12), and (2-13) results in

$$\dot{Q} = \oiint \rho \left(h + \frac{\|v^2\|}{2} + gz \right) (\vec{V} \cdot \hat{n})\, dA \tag{2-14}$$

Further, (2-14) may now be separated into the three component control surfaces of the system: the outlet surface, the inlet surface, and the inner tube surface (Figure 2-2)

$$\begin{aligned} \dot{Q} = & \oiint \rho \left(h + \frac{\|\vec{v}^2\|}{2} + gz \right) (\vec{v} \cdot \hat{n})\, dA_{tube} \\ & + \oiint \rho \left(h + \frac{\|\vec{v}^2\|}{2} + gz \right) (\vec{v} \cdot \hat{n})\, dA_{outlet} \\ & + \oiint \rho \left(h + \frac{\|\vec{v}^2\|}{2} + gz \right) (\vec{v} \cdot \hat{n})\, dA_{inlet} \end{aligned} \tag{2-15}$$

Density can be taken as constant because the fluid being discussed is water and is not expected to change phases. Observing conservation of mass,

$$\rho v A = constant \tag{2-16}$$

and taking the area of the inlet and outlet as constant, the velocity can now be taken as constant. Now, heat transfer rate may be determined in terms of the mass flow rate, $\dot{m}$.

$$\dot{Q} = \dot{m}_{outlet} \left(h + \frac{\|\vec{v}^2\|}{2} + gz \right)_{outlet} + \dot{m}_{inlet} \left(h + \frac{\|\vec{v}^2\|}{2} + gz \right)_{inlet} \tag{2-17}$$

The definition of specific enthalpy for water is

$$h = CT \tag{2-18}$$

where C is the specific heat capacity of water and T is the temperature of the water.

So, taking velocity, and mass flow rate as constant between the inlet and the outlet, along with (2-18), temperature change as a function of heat transfer rate, mass flow rate, and specific heat capacity may be determined. Additionally, because the inlet and the exit are located at the same height, the potential energy term may be neglected.

$$\dot{Q} = \dot{m}(h_{outlet} - h_{inlet}) \tag{2-19}$$

or

$$\dot{Q} = \dot{m}C(T_{outlet} - T_{inlet}) \tag{2-20}$$

$$(T_{outlet} - T_{inlet}) = \frac{\dot{Q}}{\dot{m}C} \tag{2-21}$$

Although Equation (2-21) gives no information on local heating inside the insertion arm, it is a simple formula that may be used to predict the overall performance of the cooling system.

2.2.2 Surface Heat Flux

Although analytical solutions are available for stagnation point heat flux in the hypersonic regime, the heat flux distribution on complicated surfaces still presents a challenge. Additionally, the determination of the flow conditions themselves present a difficulty. For example, it is well-known that arc-jet facilities have a coring effect in the nozzle where the peak enthalpy along the nozzle centerline can be as much as twice the bulk enthalpy thus further complicating the heat flux estimations [5, 6].

Fay & Riddell [15] developed an analytical model used to calculate the stagnation point heat flux in the hypersonic regime. For an axisymmetric body:

$$\dot{q}_s = 0.76Pr^{-0.6}(\rho_e\mu_e)^{0.5}\sqrt{\left(\frac{du_e}{dx}\right)_s}(h_{s_e} - h_w) \tag{2-22}$$

where $\dot{q}_s$ is the stagnation point heat flux, Pr is Prandtl number, ρ_e is the density at the boundary layer edge, μ_e is the viscosity at the boundary layer edge, $\left(\frac{du_e}{dx}\right)_s$ is the stagnation point velocity gradient, h_{s_e} is the specific stagnation enthalpy at the boundary layer edge, and h_w is the enthalpy at the wall. An estimate for the stagnation point velocity gradient can be obtained using Newtonian theory [16]. This results in an expression for stagnation point velocity gradient in the form:

$$\left(\frac{du_e}{dx}\right)_s = \frac{1}{R_n}\sqrt{\frac{2(p_e - p_\infty)}{\rho_e}} \tag{2-23}$$

where R_n is the nose radius, p_e is the pressure at the boundary layer edge, and p_∞ is the free stream pressure before the shockwave. Zoby [17] introduced an empirical approach to estimating the stagnation point heat flux on a blunt body in high-speed flow. The relation for stagnation point heat flux of an axisymmetric body is given by:

$$\dot{q}_s = \frac{K_i(h_{s_e} - h_w)}{\sqrt{\frac{R_{eff}}{p_s}}} \tag{2-24}$$

where K_i is a heat transfer coefficient determined empirically for several gases, p_s is the stagnation pressure, and R_{eff} is the effective nose radius. In a separate work, Zoby [16] also showed that for non-hemispherical bodies an equivalent effective radius can be used instead. In this work the author determined an effective radius, R_{eff} , using the nose radius, R_n, body radius, R_b, and corner radius, R_c, for use in stagnation point heating calculations (Figure 2-3).

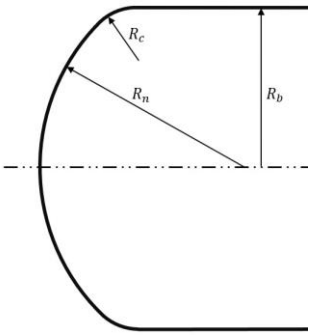

Figure 2-3: Notional blunt body with labeled radii.

In both equations (2-22) and (2-24), the stagnation point enthalpy is used, which can vary significantly from bulk enthalpy due to coring effects. Both equations (2-22) and

(2-24) are valid for axisymmetric bodies. For cylindrical bodies in a cross-flow, the Fay-Riddell [15] and Zoby [17] expressions are respectively:

$$\dot{q}_s = 0.756 Pr^{-0.6} (\rho_e \mu_e)^{0.5} \sqrt{\left(\frac{du_e}{dx}\right)_s} (h_{s_e} - h_w) \tag{2-25}$$

$$\dot{q}_s = \frac{0.75 K_i (h_{s_e} - h_w)}{\sqrt{\frac{R_{eff}}{p_s}}} \tag{2-26}$$

While these equations provide the stagnation point heat flux, some additional assumptions are required to determine the total thermal power into the insertion system. The most conservative approach would be to apply the stagnation point heat flux across the projected area of the structure exposed to the flow.

Although this approach can result in particularly conservative thermal power estimations, it can be applied in situations when the design constraints are not severe. For example, in the Mach 6 configuration at the ONR-UTA Arc-Heated Wind Tunnel, the thermal power is relatively small due to lower stagnation pressures and larger effective radius, R_{eff}. Additionally, due to the larger nozzle exit compared to Mach 4, blockage constraints allow more room for cooling passages.

$$\dot{Q}_{strut} = \dot{q}_s A_{strut} \tag{2-27}$$

where $\dot{Q}_{strut}$ is the thermal power on the strut and A_{strut} is the projected frontal area of the strut. When more stringent requirements are present, this simple approach produces overly conservative thermal power estimates, and a more refined model is required. For example, the Mach 4 arm was treated differently due to higher heating rates and less available space for the cooling system.

A possible approach to this more refined analysis, is to divide the insertion arm into two regions as shown in Figure 2-4. Region I, the instrument holder and Region II is the exposed portion of strut.

Region I is modeled as the extension of a generic, uncooled blunt body with the same external diameter attached to it (shown in Figure 2-5). This allows the heat flux on the instrument holder to be estimated from the stagnation point heat flux on the blunt body.

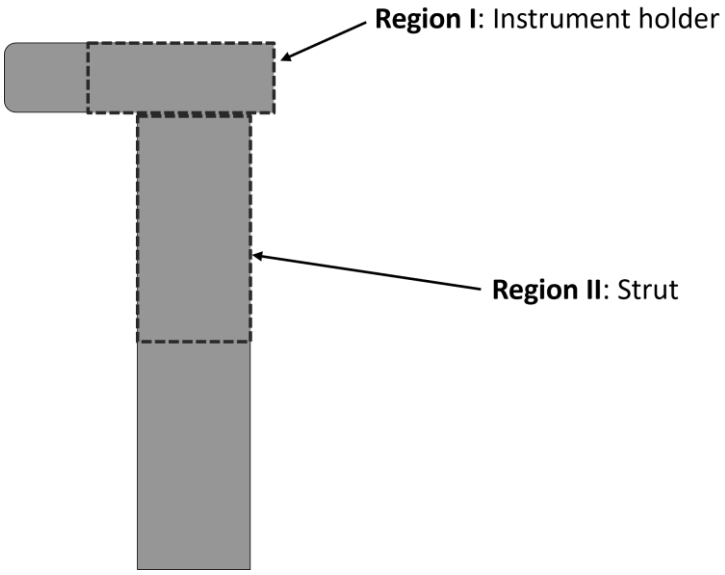

Figure 2-4: Analysis regions on insertion arm (not to scale).

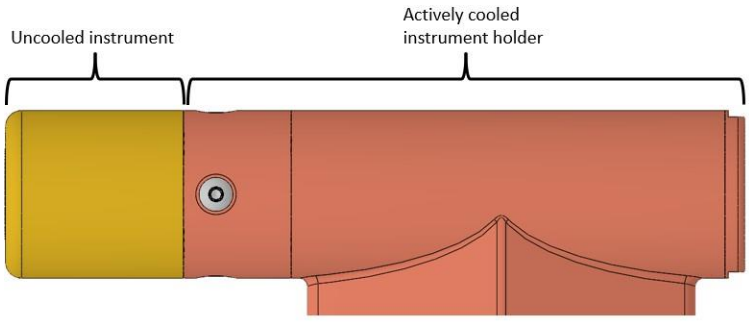

Figure 2-5: Uncooled and cooled regions of Mach 4 arm.

Smith [19] compares calculated and measured solutions to the local heat flux $\dot{q}$ on a blunt body as a function of stagnation point heat flux $\dot{q}_s$, the curvilinear distance along the surface of the body x, and the body radius R_B. Smith's calculations end at a distance x/R_B of 1.6, well before the beginning of the instrument holder. The ratio $\dot{q}/\dot{q}_s$ is 0.15 at this point and trending downward, so it is reasonable to assume that the local heat flux in the instrument holder does not exceed 15% of the stagnation point heat flux. The heat flux on the instrument holder may be estimated as:

$$\dot{Q}_{holder} = 0.15\dot{q}_s A_{holder} \tag{2-28}$$

where A_{holder} is the exposed surface area of the instrument holder.

A different approach is used to treat region II. Although the heating profile depends on the specific strut geometry, the leading edge will generally be a blunt body. Gökçen [20] provides a 2-dimensional computational analysis of the heat flux distribution on 20° wedge with a cylindrical leading edge (Figure 2-6). By scaling the stagnation point heat flux and integrating the heating profile over the surface, the total heating on the insertion arm can be estimated. The Mach 4 arm presented in this manuscript, a 20˚ half-angle diamond profile with a 0.125 in radius blunted leading edge, is used as an example (Figure 2-6).

Using this geometry, for a stagnation point heat flux of $\dot{q}_s = 1\,W/cm^2$, there is a heating per unit length of $\dot{Q}'_{ref} = 1.562\,W/cm$. A relation to the insertion arm heating may then be constructed as

$$\frac{\dot{q}_{ref}}{\dot{Q}'_{ref}} = \frac{\dot{q}_s}{\dot{Q}_{strut}/L_{strut}} \tag{2-29}$$

or

$$\dot{Q}_{strut} = \dot{q}_s L_{strut} \frac{\dot{Q}'_{ref}}{\dot{q}_{ref}} \tag{2-30}$$

where L_{strut} is the length of the strut exposed to the plume.

This numerically computed heat flux profile was compared with analytical solutions for a flat plate such as the reference temperature method [16]. The reference temperature method is an approximate method that can be used for predicting heat transfer in hypersonic flows. In this method, the heat-transfer coefficient C_H, the Reynold's number Re_x, Prandtl number Pr, and density ρ are evaluated at a reference temperature T^* such that

$$C_H^* = \frac{0.332}{\sqrt{Re_x^*}}(Pr^*)^{-2/3} \tag{2-31}$$

$$Re_x^* = \frac{\rho^* u_e x}{\mu^*} \tag{2-32}$$

$$Pr^* = \frac{\mu^* c_p^*}{k^*} \tag{2-33}$$

where u_e is the velocity at the edge of the boundary layer, x is the distance along the flat plate , c_p^* is the specific heat at constant pressure evaluated at T^*, and k^* is the thermal conductivity evaluated at T^*. The reference temperature is a function of the Mach number at the edge of the boundary layer M_e, the temperature of the wall T_w, and the temperature at the edge of the boundary layer T_e such that

$$T^* = T_e\left[1 + 0.032M_e^2 + 0.58\left(\frac{T_w}{T_e} - 1\right)\right] \tag{2-34}$$

The local heat flux for the flat portion of the strut can then be estimated as

$$\dot{q} = \rho^* u_e C_H^*(h_{aw} - h_w) \tag{2-35}$$

where h_{aw} is the enthalpy for the adiabatic wall and h_w is the enthalpy at the wall. Note that this is an approximate method intended for flow over a flat plate. Because the actual strut geometry has a cylindrical leading edge, this method should be expected to have poor accuracy near the cylindrical leading edge and improved (but still not exact) accuracy further away from the leading edge.

The values from the scaled heat flux profile method and the reference temperature method were compared at various locations along the flat portion of the strut surface and is reported in Figure 2-6. While the reference temperature method underestimates the heat flux compared to the scaled heat flux profile method, it nevertheless provides a good initial estimate of the heat flux. However, the insertion arm cooling system was designed using the thermal loads from the scaled heat flux profile method.

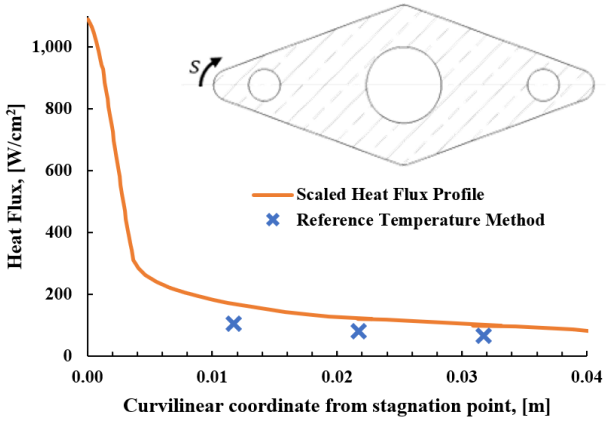

Figure 2-6: Heat flux distribution on Mach 4 strut.

Table 2-1 Insertion arm strut geometry

Geometry	Mach 6	Mach 4
Nose Radius, R_N, cm	4.03	0.32
Strut Length, L_{strut}, cm	18.42	5.08

The arc-jet test conditions used for the design (with air as a test gas) are shown in Table 2-2. The corresponding thermal loads for design conditions are shown in

Table 2-3. The heating conditions are at a bulk enthalpy of 10 MJ/kg and with the instrument centerline located at the top edge of the nozzle exit. In this scenario, L_{strut} is the exit diameter of the nozzle minus the radius of the calorimeter. Additionally, the full heating on the instrument holder is considered, although the instrument is halfway removed from the plume.

Table 2-2 Summary of design conditions

Property	Mach 6	Mach 4
Freestream Pressure, p_∞, Pa	94	1875
Stagnation Pressure, p_s, kPa	5.2	45
Bulk Enthalpy, h_0, MJ/kg	10	10

Table 2-3 Summary of calculated thermal loads for design conditions

	Property	Mach 6	Mach 4
Fay-Riddell [15]	$\dot{q}_{strut}, W/cm^2$	83	827
	$\dot{q}_{total}, W/cm^2$		274
	$\dot{Q}_{strut}, kW$	10.3	8.3
	$\dot{Q}_{holder}, kW$		3.1
	$\dot{Q}_{total}, kW$	10.3	11.4
Zoby [17]	$\dot{q}_{strut}, W/cm^2$	105	1063
	$\dot{q}_{total}, W/cm^2$		349
	$\dot{Q}_{strut}, kW$	13.0	10.7
	$\dot{Q}_{holder}, kW$		3.9
	$\dot{Q}_{total}, kW$	13.0	14.6

2.2.3 Cooling System Performance

The final result of the control volume analysis in (2-23) may be used to estimate to cooling water temperature increase:

$$T_{out} - T_{in} = \dot{Q}_{total}/\dot{m}C \tag{2-36}$$

Where $\dot{Q}_{total}$ is reported in

Table **2-3** for the two nozzle configurations. With a measured flow rate of 5.5 liters per minute (for the Mach 4 arm), a maximum temperature change of 33 K was estimated (Figure 2-7). For the Mach 6 arm, due to the larger cooling passages, the flow rate was measured to be 26.5 liters per minute. This corresponds to a maximum estimated temperature change of 6 K. The performance can be verified through temperature measurements at the inlet and outlet, along with a measurement of the flow rate.

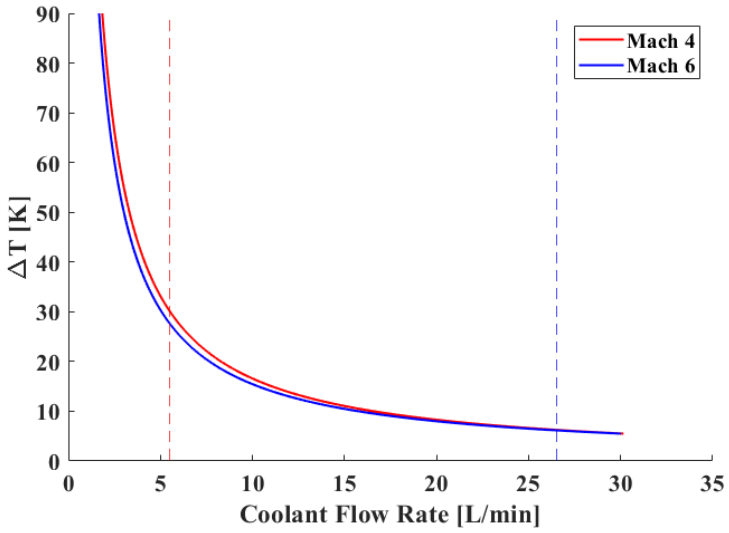

Figure 2-7: Predicted temperature change as a function of coolant flow rate in Mach 4 insertion arm.

2.3 Aerodynamic Loads

Being certain of the location of the instrument mounted on the arm relative to the centerline of the arc-jet plume is critical to all intrusive diagnostics and testing. However, aerodynamic loads for the design arc-jet run conditions (Table 2 2) were determined not to be a primary driver in the overall structural design of the insertion system. The aerodynamic loads were determined through a modified shock-expansion analysis, whereas the corresponding structural deflections were determined through a 2-dimensional frame analysis tool.

If deflection of the arm is significant enough, then the instrument or test article may deviate unacceptably from its nominal position in the plume, with unacceptable aerodynamic deflection being defined as ±1mm. Thus, it is important to determine the aerodynamic loads and the response to the loads during arc-jet operations.

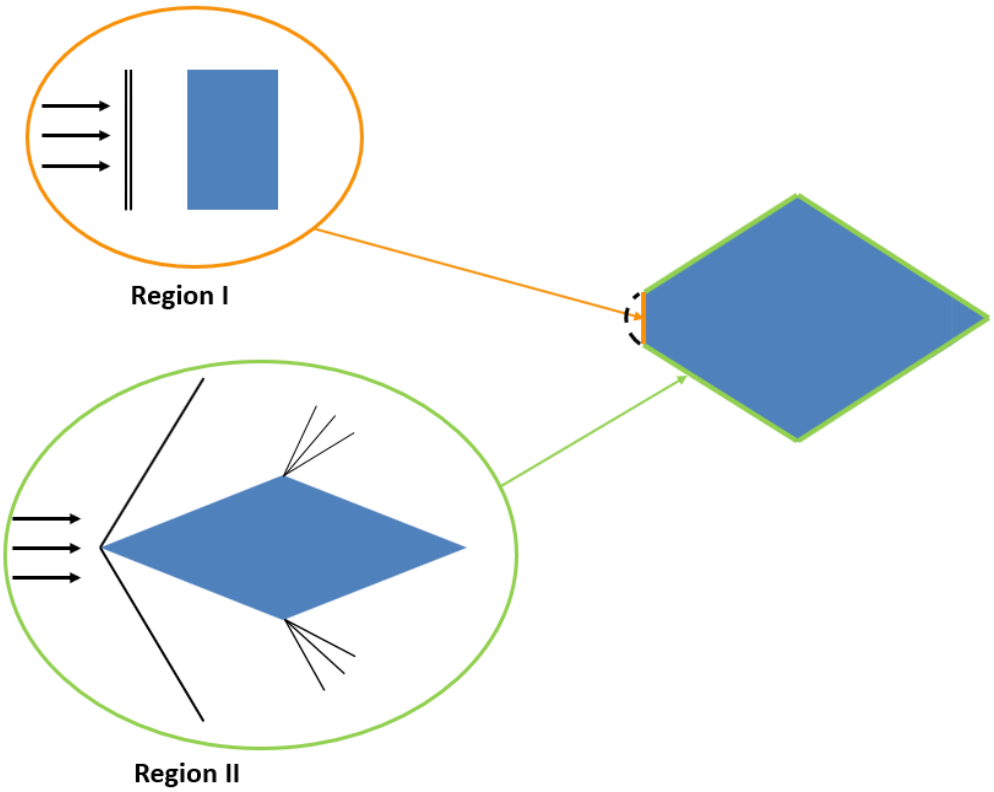

Figure 2-8: Regions for aerodynamic analysis.

The aerodynamic effects of hypersonic flow around the Mach 4 insertion arm's profile are complex and several simplifying assumptions must be made. Without these simplifying assumptions, a complex and resource-intensive computational analysis is required. The actual diamond shape with a cylindrical leading edge is simplified into a diamond shape with a flat leading edge (Figure 2-8). Then, Regions I and II are analyzed separately. Region I is treated as a flat face perpendicular to the flow, and therefore the stagnation pressure after a normal shock is applied on the entirety of this region's surface. Region II is analyzed as a diamond shape with a sharp leading edge, with an attached oblique shock at the leading edge and Prandtl-Meyer expansion fans on either side. The axial components of the pressure applied to each region are then summed as the drag force, shown in Figure 2-9 and equation (2-37).

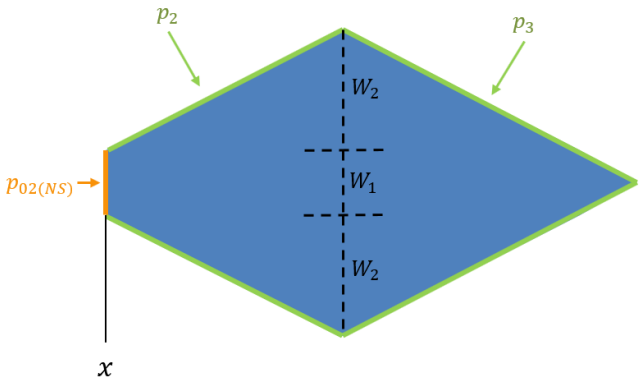

Figure 2-9: Shock-expansion analysis.

$$D' = W_1 p_{02(NS)} + 2W_2 p_2 - (W_1 + 2W_2) p_3 \qquad (2\text{-}37)$$

In these calculations, calorically perfect gas assumptions are used instead of thermally perfect, equilibrium, or non-equilibrium assumptions. This is because the pressure distribution is relatively insensitive to the effects of chemical reactions [16].

Not considered are thermal expansion effects: because there is significant heating on the leading edge of the insertion arm compared to the trailing edge, it could be expected that thermal expansion in the leading edge could compound the mechanical deflection at the tip of the arm. However, if the cooling system is functioning normally, it is expected that the highest temperatures in the leading edge will be limited to a relatively small region.

Additionally, the aerodynamic load of the instrument must be included. Again, a simplifying assumption was made applying $p_{02(NS)}$ over the front surface of the calorimeter, resulting in an axial load of 12.7 lbf at the tip of the Mach 4 insertion arm and a 5.3 lbf axial load on the tip of the Mach 6 insertion arm. Lastly, due to the lower pressures in the Mach 6 plume, the drag force on the Mach 6 arm is simply modeled as the stagnation pressure applied over the entire projected area of the strut and calorimeter. Figure 2-10 shows the loading for the Mach 4 and Mach 6 arms when mounting the slug calorimeter and raising the calorimeter to the top of the respective nozzle exit for worst-case loading conditions.

Once the aerodynamic loads are determined, a mechanical analysis to determine elastic deflection is necessary. Although a complex finite-element analysis would be the most accurate, a simple solution is again sought. The insertion arm is modeled as a simple cantilevered beam with a distributed load along the strut portion and a point load at the mounting point for the instrument. FTool is then used to determine deflections at the instrument location. Deflections due to the loads in Figure 2-10 are shown in Figure 2-11.

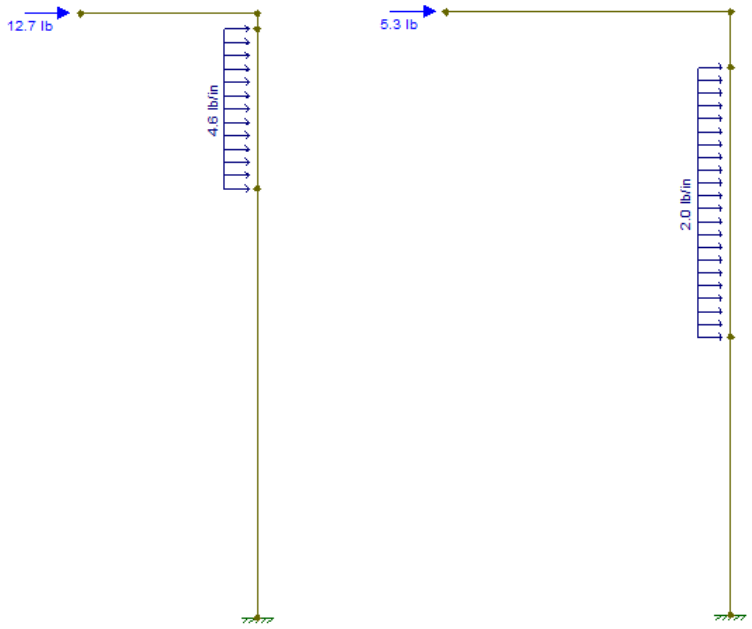

Figure 2-10: Aerodynamic loads on (a) Mach 4 arm and (b) Mach 6 arm.

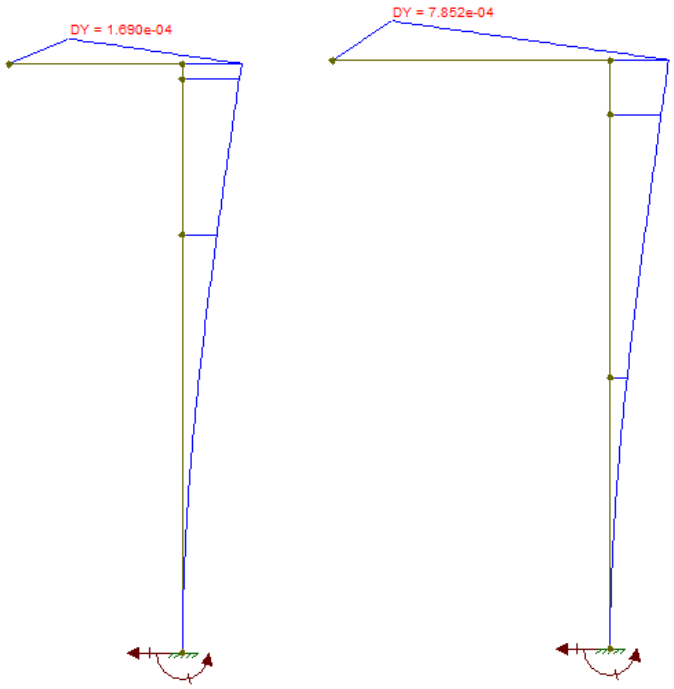

Figure 2-11: Aerodynamic deflection away from flow centerline (in inches) in (a) Mach 4 arm and (b) Mach 6 arm.

Chapter 3

Modular Platform Design

The platform consists of three subsystems: the carriage, the insertion arms, and the connected test articles. The carriage subassembly provides the base and active motion capability of the platform. The insertion arms are connected to the carriage and provide a mounting point for instruments and test articles along with internal passages for instrumentation. The platform is additionally wrapped in a layer of silicate cloth (Figure 3-1) minimize the potential for thermal damage to the carriage.

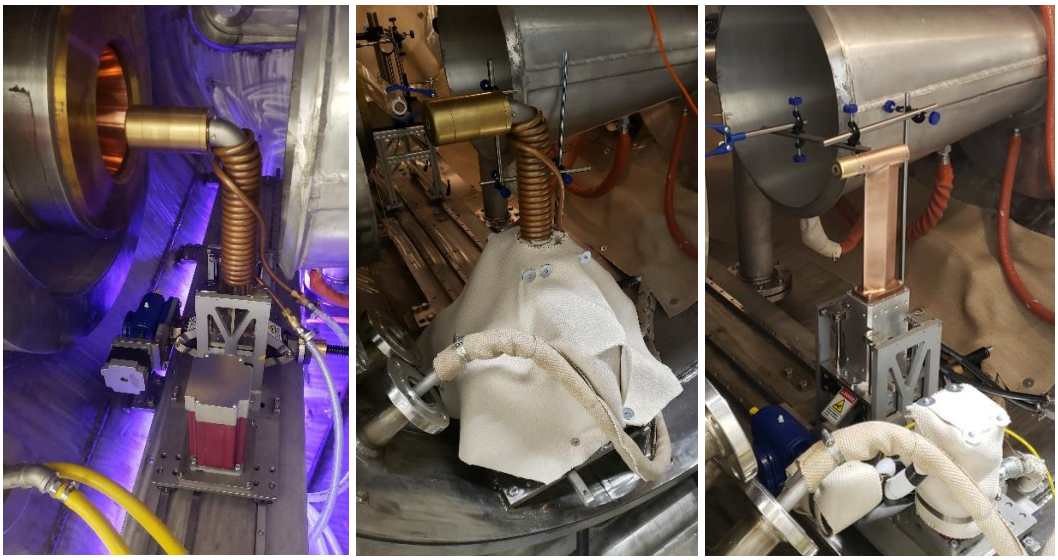

(a) **(b)** **(c)**

Figure 3-1: Assembled insertion platform. (a) Complete platform with Mach 6 arm mounted, (b) complete platform with Mach 6 arm and thermal blankets mounted, and (c) complete platform with Mach 4 arm and partial thermal blanket installation.

3.1 Early Designs

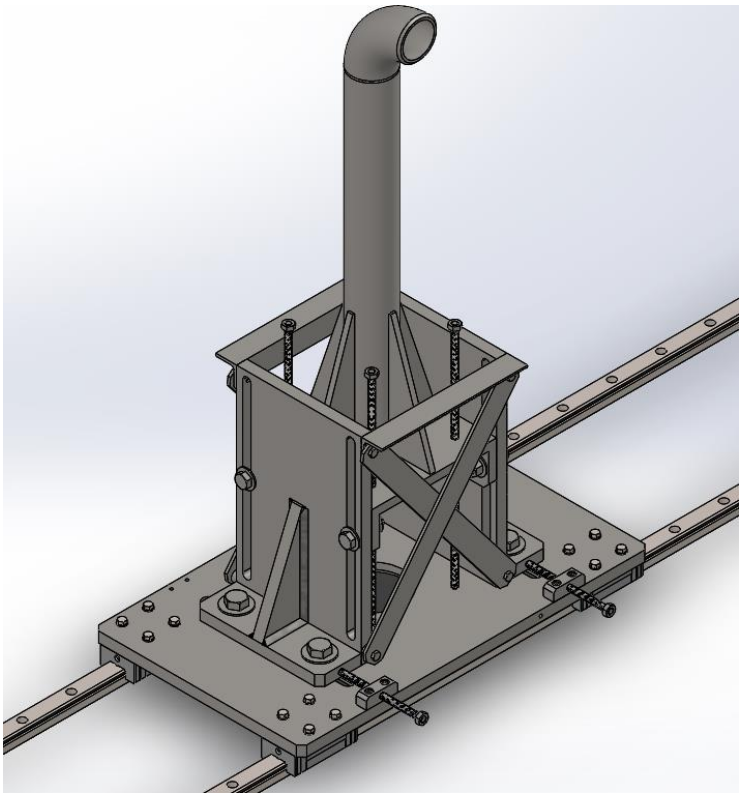

Figure 3-2: Early platform design.

The early insertion platform design (Figure 3-2) was focused on determining the basic layout and motion mechanisms. The vertical and axial position would be set by hand using a series of screws, and the lateral axis was the only actively controlled axis of motion. At this earliest stage, the 20mm rail and bogie layout was selected for the lateral motion and would carry over to the final design, along with the axial adjustment mechanism.

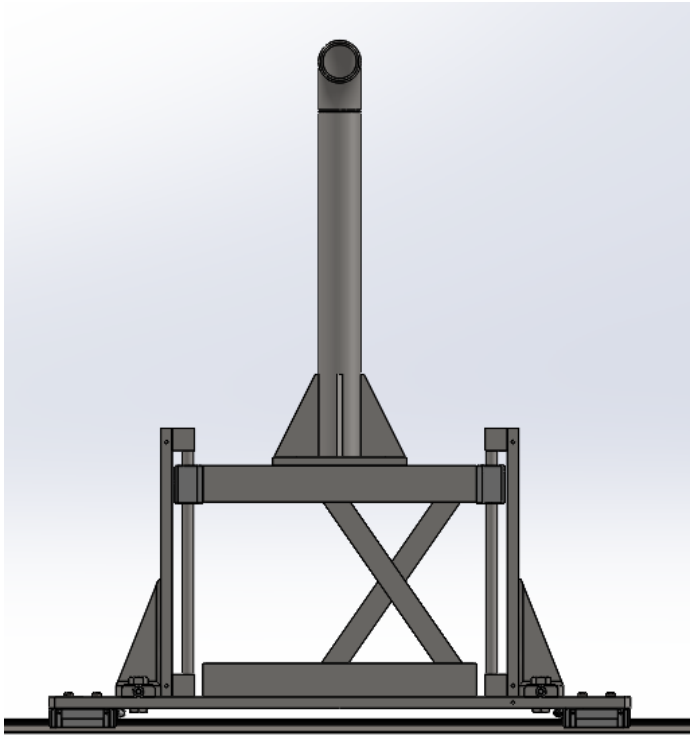

Figure 3-3: Early platform design with vertical motion mechanism.

Only one axis of motion limits the capabilities of the platform, so including active control of the vertical motion was included as a design requirement in the next design iteration. This would allow for off-axis positioning for instruments like the shear wedge, and full 2-dimensional characterization of the plume. The mechanism would need to be compact to operate in the confines of the test section, allow for the vertical motor to be located relatively far away from the plume to prevent thermal damage to motor or motor cables, and must be relatively stiff to limit deflection of the test article during the run.

A new mechanism was then designed which used a scissor jack and four vertical guide rails (Figure 3-3). The folding scissor jack is compact and keeps the motor and mechanism at or below the arm itself (as opposed to a rack and pinion, where the rack would remain exposed to the plume). The guide rails decouple the moments and the lateral/

axial forces on the arm from the vertical motion mechanism and keep the arm stiff during operation.

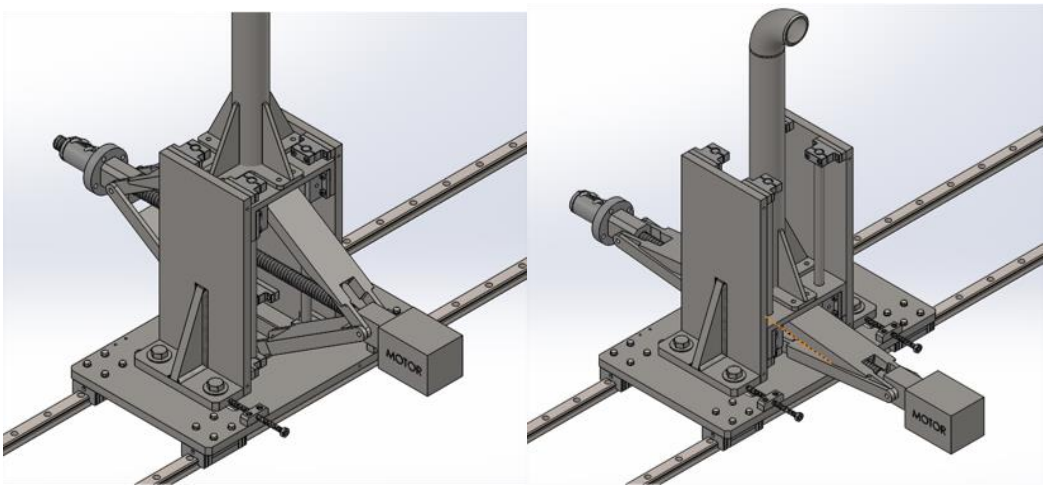

(a) (b)

Figure 3-4: Early platform design with improved scissor jack mechanism at the (a) raised and (b) lowered positions.

The scissor jack concept was further improved upon by rotating the mechanism. The scissor jack would then be actuated by a worm screw through the center, itself operated by a direct connection to a stepper motor. This greatly reduces the lateral size of the platform and allows for symmetric loading to reduce the potential for tilting the arm under load. ½ inch diameter guide rails and bearings were also selected at this stage.

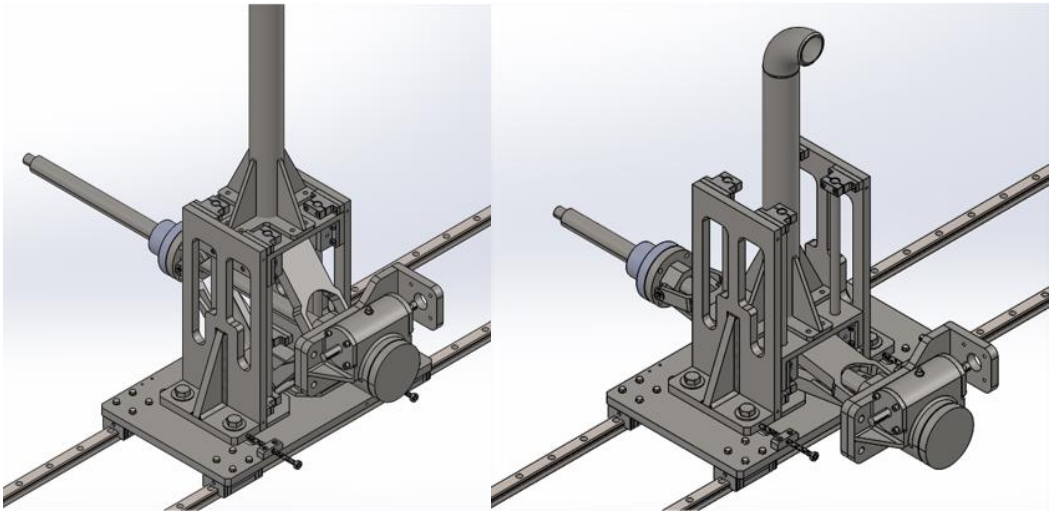

(a) (b)

Figure 3-5: Early platform design with added screw jack and reduced scissor jack dimensions at the (a) raised and (b) lowered positions.

In order to reduce the size of the motor required, a gear reduction mechanism was implemented. The Nook Industries ActionJac with a 24:1 gear ratio, 1 inch diameter acme screw, and 90° turn for the input shaft was selected. This allows for a smaller motor to lift the arm at the expense of vertical motion speed. The reduced vertical speed does not significantly degrade the platform's capabilities because, as mentioned, the vertical axis is not the insertion axis.

Further changes were made as well, as seen in Figure 3-5. The scissor jack members were shortened to reduce the overall dimensions of the platform and allow for clearance with the worm acme screw, and the base of the scissor jack was coupled to the side plates for axial adjustment. Material was removed from the side plates to reduce mass and therefore limit the secondary motions during the lateral insertion movement.

As the insertion platform design converged, alternate methods of lateral actuation were studied in order to reduce costs and development time. An actuation system was developed which would allow insertion to the centerline using a pneumatic cylinder

attached to the test section baseplate and the carriage baseplate (Figure 3-6). This actuation method fails to meet a key requirement of the design: velocity profile control across the nozzle plume. Nevertheless, many types of experiments may be conducted with stationary test articles at the flow centerline, so the pneumatic actuation capability has been retained in the final design as a back-up insertion method. In the case that the lateral motor fails, the pneumatic cylinder may be quickly installed to reduce downtime of the *Leste* facility.

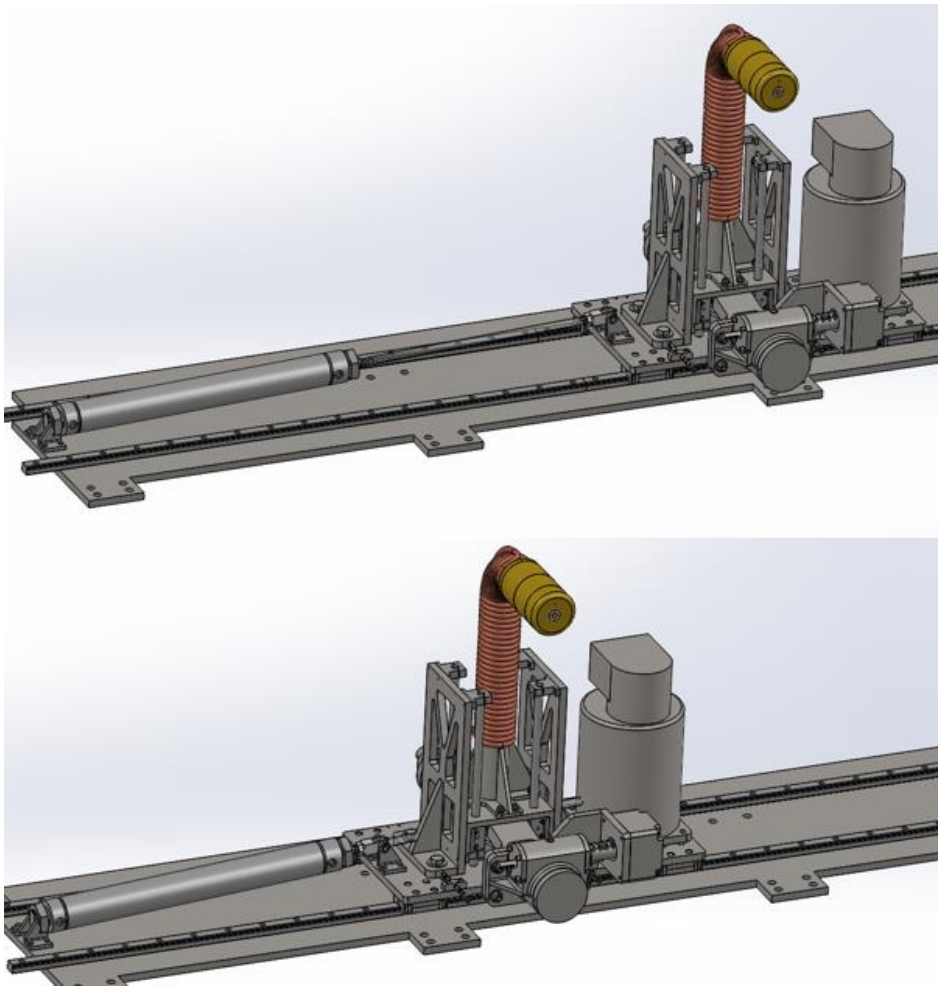

Figure 3-6: CAD assembly of insertion platform using pneumatic actuation.

3.2 Carriage Design

The carriage provides a stiff and stable platform for the insertion arm and the test articles. It provides active and remotely controlled vertical and lateral motion and allows for manual adjustment of the axial distance. The actuators are placed on a compact, self-contained platform, mounted on linear rails using low-friction ball-bearing carriages with minimal free play. Stepper motors for both lateral and vertical motion were selected due to their accuracy. This 2-axis motion allows the platform to satisfy the requirement for full nozzle exit plane characterization.

3.2.1 Scissor Jack Design

The scissor jack is designed to be a robust and compact mechanism to raise and lower the insertion arm. Because the mechanism folds in on itself when it lowers, it preserves valuable test section space.

Figure 3-7 shows the assembly details of the scissor jack. The flange adapter (item 1), located at the top, mounts the insertion arm subassembly. Below the flange adapter, the scissor jack members (item 2) transfer the load to the travel nut mount (item 3), the vertical drive adapter (item 4), and the baseplate. The travel nut mount and vertical drive adapter connect to the travel nut and screw jack (item 5) respectively. Lastly, the vertical drive motor (item 6) connects via a shaft coupler to the screw jack at a 90° angle.

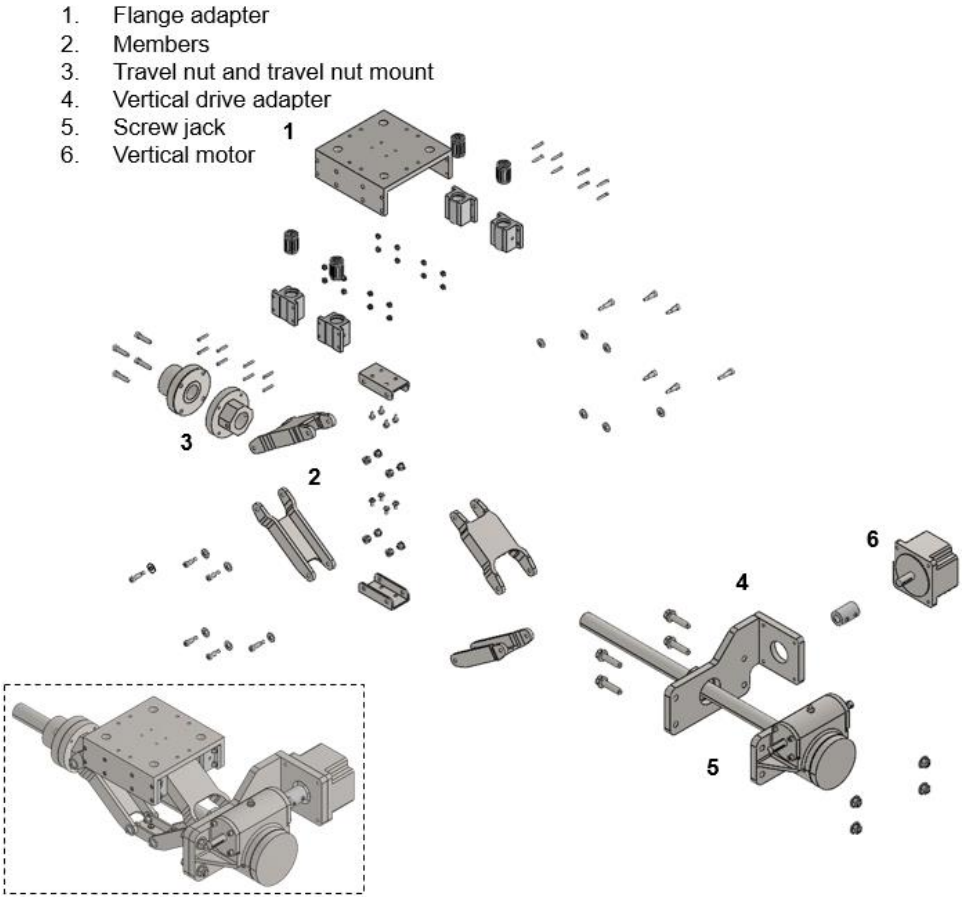

Figure 3-7: Scissor jack structural components exploded view.

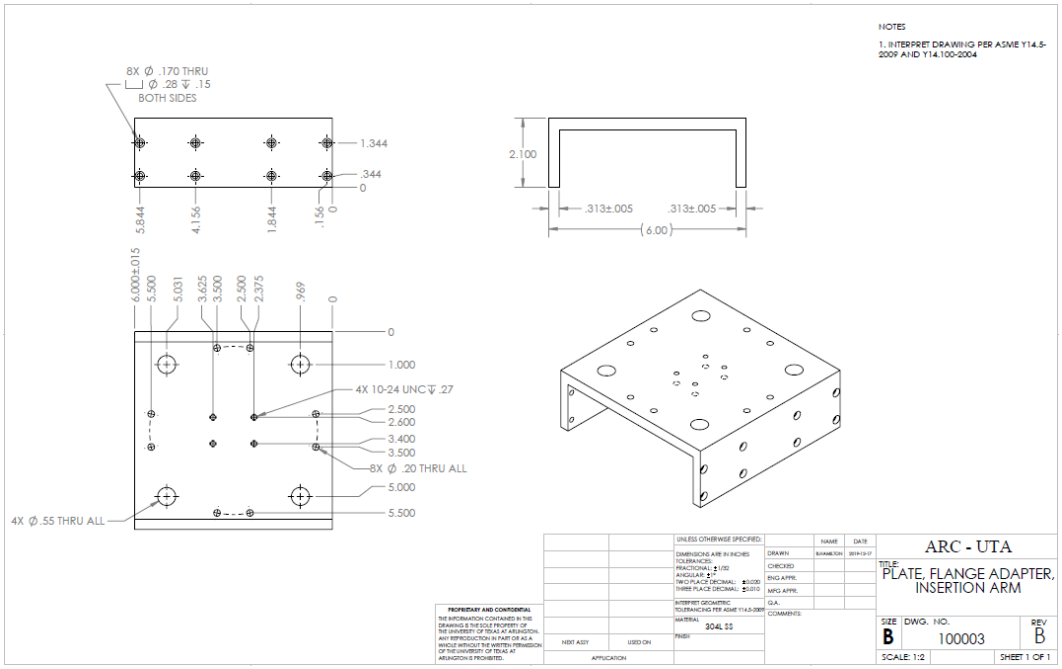

Figure 3-8: Flange adapter drawing.

The flange adapter transfers forces between the insertion arm, the scissor jack, and the guide rails. It is constructed from a 6-inch extruded c-channel to ease construction. Bearing housings are mounted to the inside face of the flange, which transfer all moments along with the lateral and axial forces to the guide rails. On the web, four clearance holes allow the guide rails to pass through. Additionally, the web uses an 8-hole pattern to mount the insertion arm, and a 4-hole pattern in the center to mount the scissor jack.

One significant concern on the flange adapter is whether the screws which attached the arm to this component (Figure 3-9) would fail in tension or by thread stripping. The Machinery's Handbook [22] offers a method for determining the length of engagement, L_e, in order to ensure failure in tension.

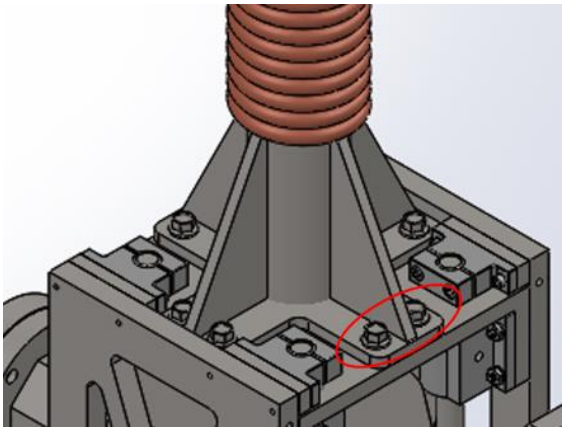

Figure 3-9: Flange adapter fasteners.

For materials with equal tensile strength, the length of engagement is given by

$$L_e = \frac{2A_t}{3.1416K_{n,max}\left[1/2 + 057735n\left(E_{s,min} - K_{n,max}\right)\right]} \tag{3-1}$$

where A_t is the tensile area of the screw, $K_{n,max}$ is the maximum minor thread diameter, $E_{s,min}$ is the minimum pitch diameter of the external thread, and n is the number of threads per inch.

The thread stripping factor J is

$$J = \frac{A_s\sigma_{UTS,ext}}{A_n\sigma_{UTS,int}} \tag{3-2}$$

where $\sigma_{UTS,ext}$ is the ultimate tensile strength of the external threads, $\sigma_{UTS,int}$ is the ultimate tensile strength of the internal threads, A_s is the shear area of the external thread, given as

$$A_s = 3.1415nL_eK_{n,max}\left[\frac{1}{2n} + 0.57735\left(E_{s,min} - K_{n,max}\right)\right] \tag{3-3}$$

and A_n is the shear area of the internal thread, given as

$$A_n = 3.1415nL_eD_{s,min}\left[\frac{1}{2n} + 0.57735\left(D_{s,min} - E_{s,max}\right)\right] \tag{3-4}$$

In (3-4), $D_{s,min}$ is the minimum major diameter of the external thread, while $E_{s,max}$ is the maximum pitch diameter of the external thread.

If J is less than or equal to one, the L_e is the minimum thread engagement to prevent thread stripping. If J is greater than 1, then the minimum thread engagement length Q is

$$Q = JL_e \tag{3-5}$$

For a #8-32 screw with a listed ultimate tensile strength of $\sigma_{UTS,ext} = 160000\,psi$ and a 304L SS plate with ultimate tensile strength $\sigma_{UTS,int} = 81800\,psi$, $J = 1.17$, so the minimum thread engagement distance is $Q = 0.145\,in$. Thus, the thickness of the flange adapter was selected as 0.313 in.

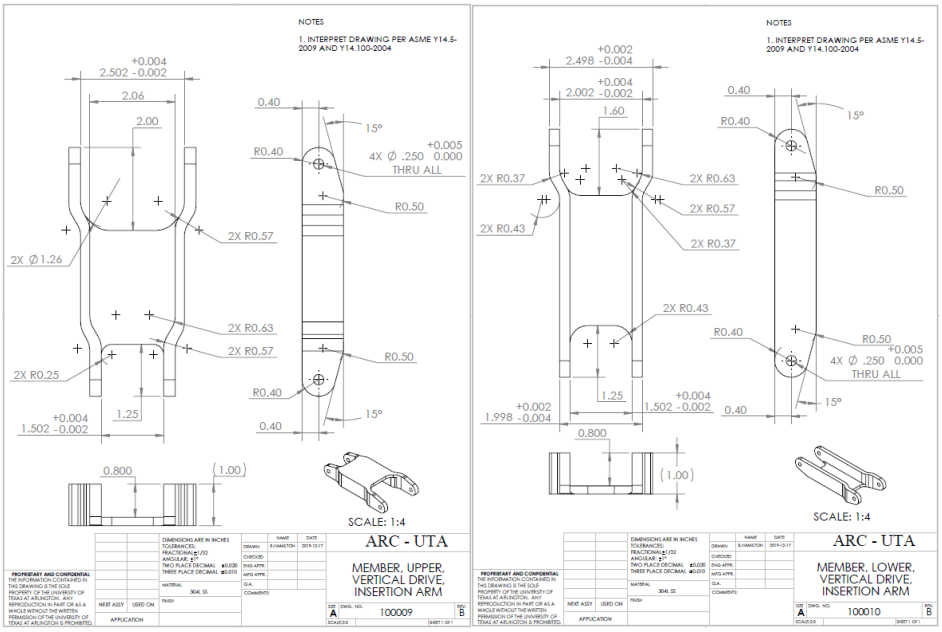

Figure 3-10: Scissor jack member drawings.

The scissor jack members, shown in Figure 3-10, are two pairs of machined stainless steel connectors which transfer the vertical loads from the insertion arm to the carriage. The arms are designed such that they nest inside each other at the scissor jack depresses. At the minimum elevation, the members are at an 11° angle with the horizontal.

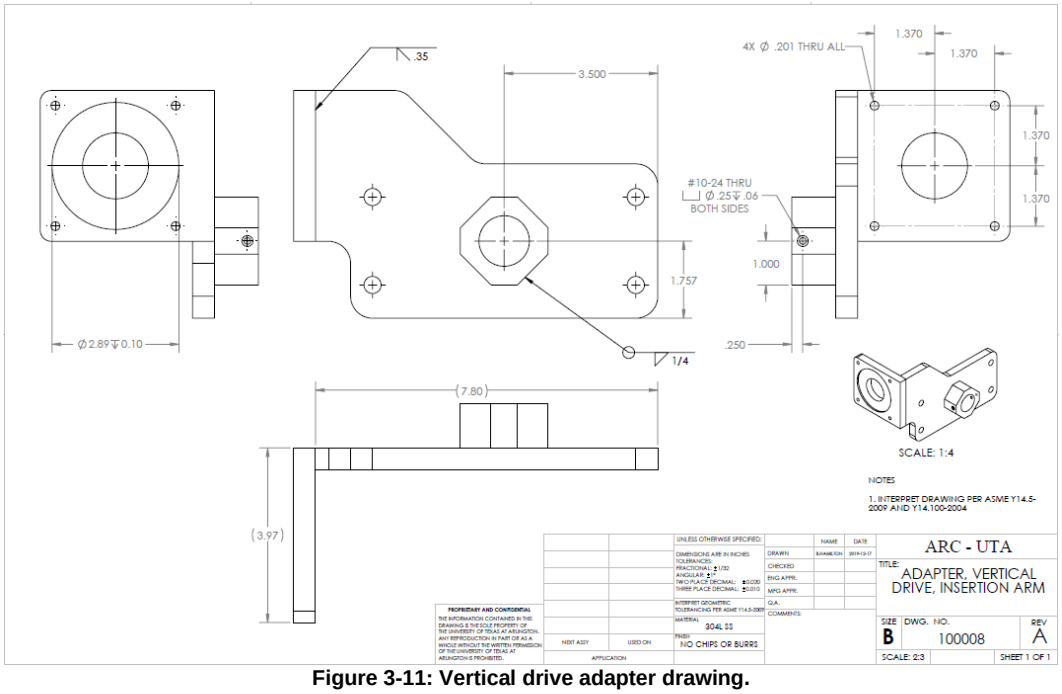

Figure 3-11: Vertical drive adapter drawing.

The vertical drive adapter, shown in Figure 3-11, transfers forces between the vertical motor, the screw jack, and the scissor jack members. It is constructed from three different plates which are waterjet cut, machined, and then welded together. The vertical motor connects via a 4-hole pattern, while the screw jack is connected perpendicularly to the motor via its own 4-hole pattern. The scissor jack member pivot about two shoulder screws on either side of the acme screw.

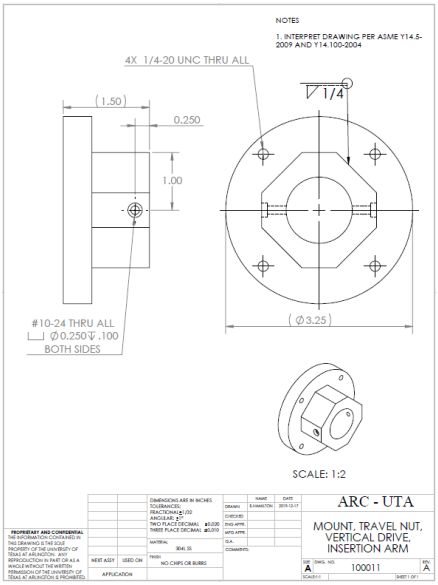

Figure 3-12: Travel nut mount drawing.

Lastly, the travel nut mount, shown in Figure 3-12, transfers mechanical loads between the scissor jack members and the screw jack's travel nut. This component is created from two waterjet cut plates of stainless steel, which are then welded together and machined. Tapped holes for shoulder screws are created in a similar fashion as the vertical drive adapter.

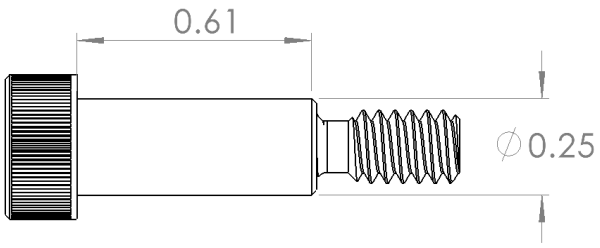

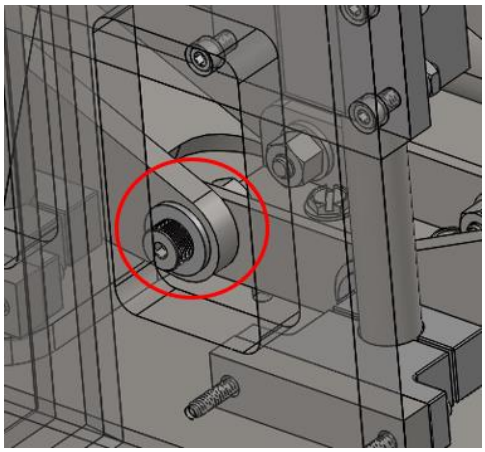

Figure 3-13: Scissor jack shoulder screw.

The shoulder screws on the scissor jack (Figure 3-13) are under significant direct shear loads and therefore require some mechanical analysis to determine the appropriate size. The shear stress expected across the four shoulder screws with the largest load is

$$F_{load} = \frac{m_{load} g}{\sin(\theta)} \tag{3-6}$$

$$F_s = 4\tau_s A \tag{3-7}$$

where A is the cross-sectional area of the shoulder screw shaft, τ_s id the material shear strength, F_s is the maximum force on the screws, m_{load} is the maximum expected mass placed on the flange adapter along with all of the scissor jack assembly mass, F_{load} is the predicted maximum load force placed on the shoulder screw shaft, θ is the angle of the scissor jack members with respect to the horizontal (Figure 3-14), and g is acceleration due to gravity [22]. Dynamic loads are neglected due to the low speed of the vertical traverse mechanism.

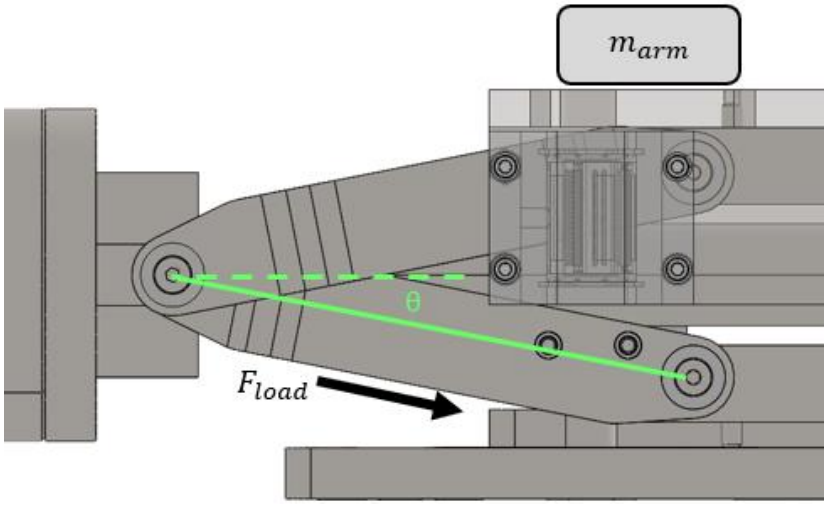

Figure 3-14: Scissor jack load angle.

For an estimated maximum mass of 160 lbm, a ¼-inch diameter shaft, manufacturer supplied minimum shear strength of 35,000 psi, and minimum load angle of $\theta = 11°$, the safety factor, SF, is expected to be

$$SF = \frac{F_s}{F_{load}} = 8.2 \qquad (3\text{-}8)$$

Because of the large safety factor, the shoulder screws are expected to stay intact even during rough handling and after future expansions which will increase the load on the shoulder screws.

3.2.2 Carriage Structural Components

The main structural components of the carriage are constructed from 304L stainless steel due to conditions inside the test section. Because of the prevalence of monoatomic oxygen in arc-jet flows, material oxidation is a serious concern for components located inside the test section. Stainless steel forms a chromium oxide passive layer [21] which inhibits oxidation corrosion. Additionally, stainless steel maintains much of its mechanical strength at elevated temperatures, making it an ideal material choice for many arc-jet applications.

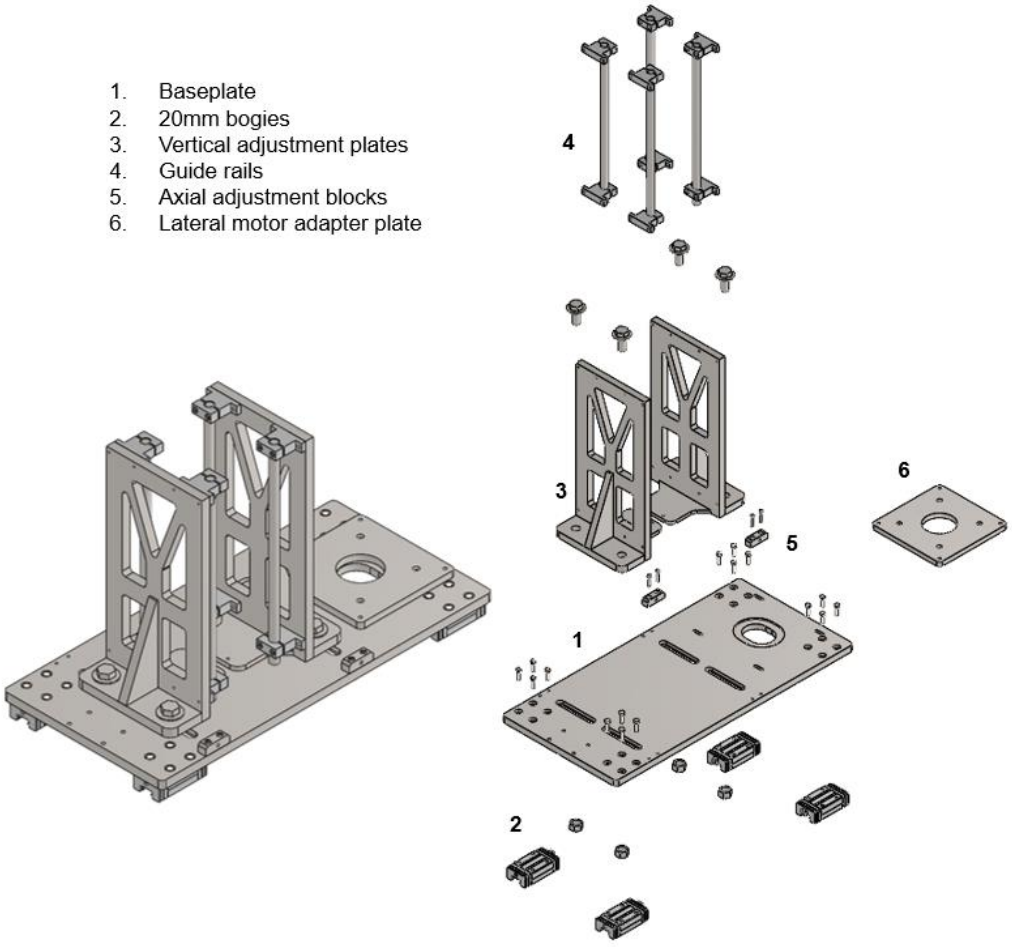

Figure 3-15: Carriage structural components exploded view.

When possible, carriage structural components were designed as 2-dimensial plates to be cut by waterjets. Waterjet cuts are inexpensive and allow complex patterns to be generated with minimal added costs. Plates were then assembled by fasteners or by welding. Figure 3-15 shows the overall design of the carriage structure.

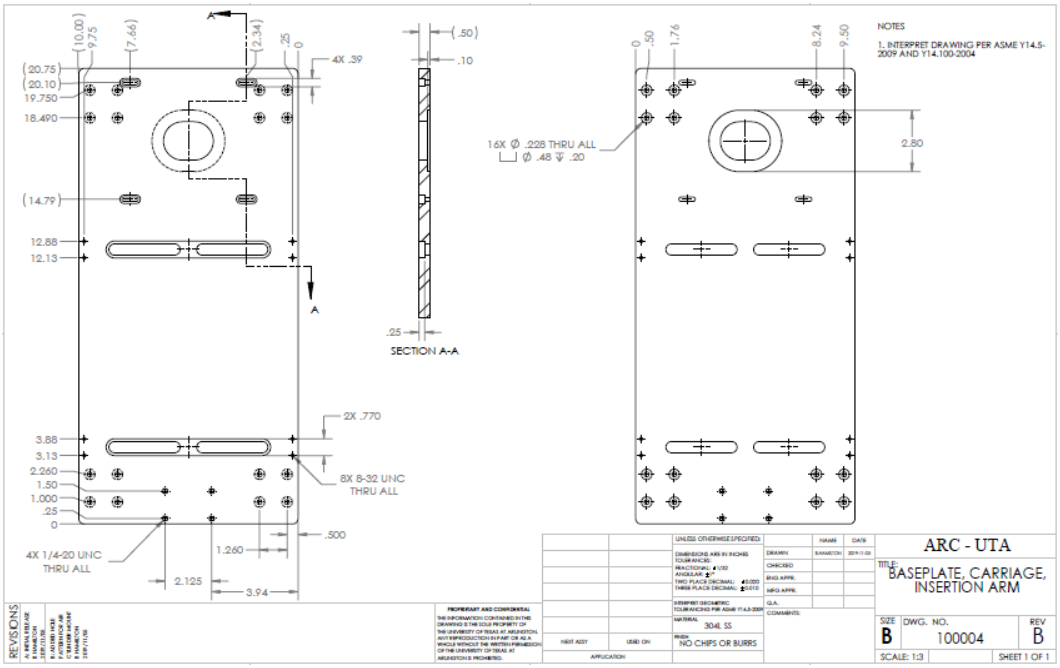

Figure 3-16: Carriage baseplate drawing.

The carriage baseplate, shown in Figure 3-16, is the main mounting location for the insertion platform. Four 20mm linear ball-bearing bogies are attached at each corner, which allow for smooth lateral motion with extremely minimal play in other dimensions. Four large slots, sized for 3/8 inch bolts, mount the vertical adjustment plates while allowing for manual adjustment in the axial direction. The bottom of the slots are recessed, allowed the use of captive nuts. Next to the vertical adjustment plate slots, the lateral motor adapter plate is mounted on smaller slots. These slots allow adjustment of the engagement distance on the rack and pinion gears. A large clearance slot allows space for the lateral motion motor shaft and pinion to pass through the baseplate. The lateral motion stepper motor is directly connected with a helical 32-tooth 50 mm diameter pinion to a rack mounted at the same level and parallel to the rails. Additionally, a ¼-20 screw hole pattern is included to allow installation of the pneumatic cylinder shown in Figure 3-6.

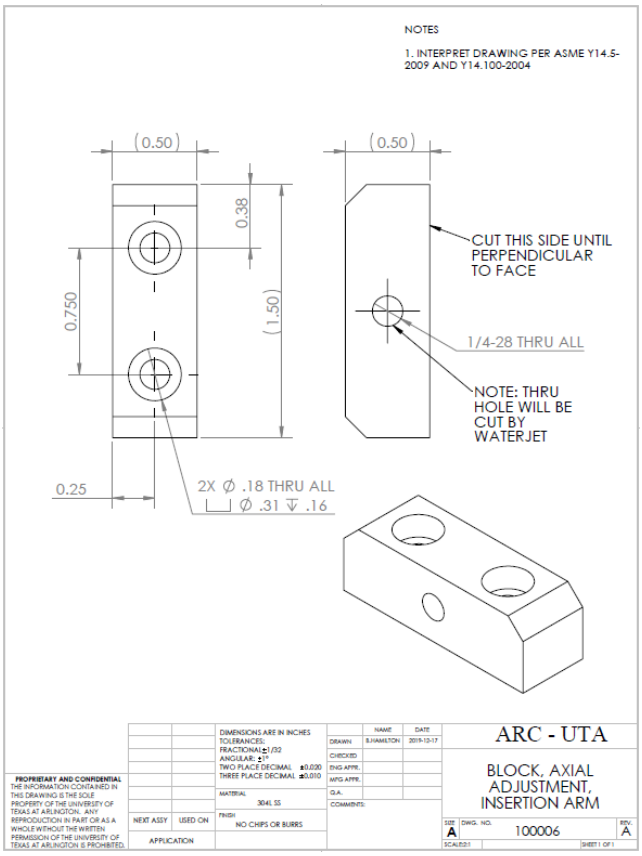

Figure 3-17: Axial adjustment block drawing.

The axial adjustment blocks, shown in Figure 3-17, allow for fine adjustment of the axial distance of the arm from the nozzle exit. By inserting a ¼-28 screw into two of these blocks, the arm can be moved along the surface of the baseplate until the desired position is reached.

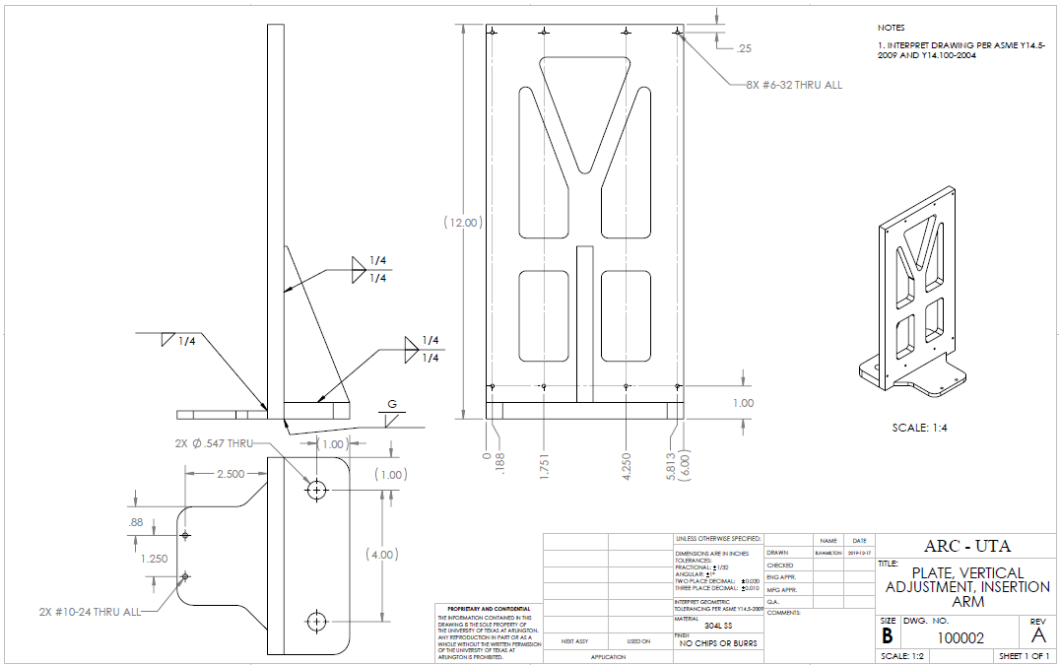

Figure 3-18: Vertical adjustment plate drawing.

The vertical adjustment plates, shown in Figure 3-18, are critical components for the functioning of the platform. The components are composed of four different plates cut by waterjet and welded together. The 12-inch plate mounts the guide rails, and has material cut out to reduce excess mass as mentioned earlier. The 2-inch plate on the bottom connects to the baseplate. The triangular rib is then welded between these two plates to strengthen this components under lateral loads (such as dynamic loads experienced during platform insertion). Lastly, a thinner plate is welded opposite the 2-inch plate as an attachment point for the scissor jack base.

3.2.3 Motor Selection

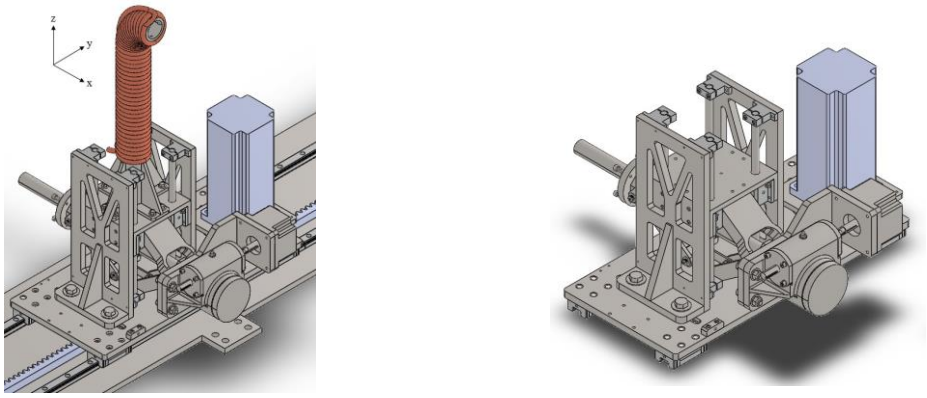

(a) **(b)**

Figure 3-19: CAD assemblies of (a) complete platform with Mach 6 arm mounted, (b) carriage subassembly.

While the vertical motion need not be fast, the mechanism must be compact and stiff, with minimal backlash in the mechanism. For compactness, a custom scissor jack was developed and shown in Figure 3-20. The scissor jack is driven by an Applied Motion HT34-504 stepper motor through a worm gear jack with a 24:1 gear ratio. A vertical motion range of ±10.16 cm from the flow centerline is possible. The mechanism is stiffened and stabilized by four precision bushings riding on stainless steel guide rails attached to the carriage base plate.

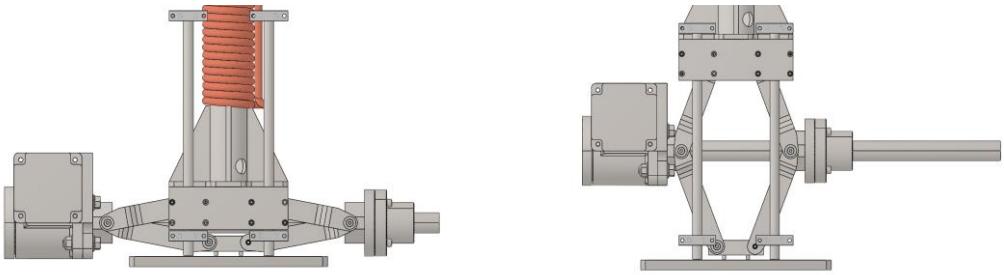

(a) **(b)**

Figure 3-20: Scissor jack mechanism located at (a) -4 inches from flow centerline, (b) +4 inches from flow centerline.

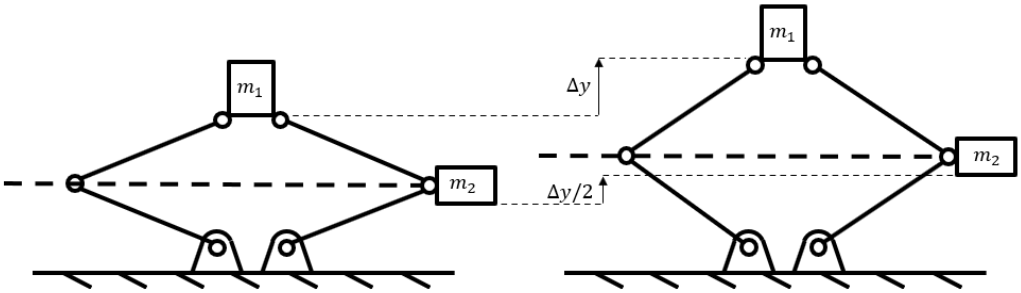

Figure 3-21: Schematic of scissor jack with fully lifted mass m_1 and half-lifted mass m_2.

To select the proper vertical stepper motor, a simplified model was developed based on a power balance between the motor and the velocity of the lifted mass.

$$\tau = \frac{gv(m_1 + m_2/2)}{\eta\omega} \tag{3-9}$$

where v is the vertical speed of the arm, m_1 is the mass lifted by the scissor jack, m_2 is the mass of the half-lifted components such as the vertical motor, screw jack, and the scissor jack itself (see Figure 3-21), ω is the rotational speed of the vertical motor, and η is the mechanical efficiency of the motor.

For a typical use situation with a 55 lbm lifted mass and 65 lbm half-lifted mass moving at 1 inch/second and a mechanical efficiency of 75%, the motor needs to rotate at 20 rev/s with a torque of 16 oz-in. Further, a starting torque of 32 oz-in is required for the screw jack. However, due to the low cost and size difference between stepper motors at this size, and the desire for a motor to potentially lift much a much larger mass in the future, the oversized Applied Motion HT34-504 stepper motor was selected. Its torque curve is reported in Figure 3-22.

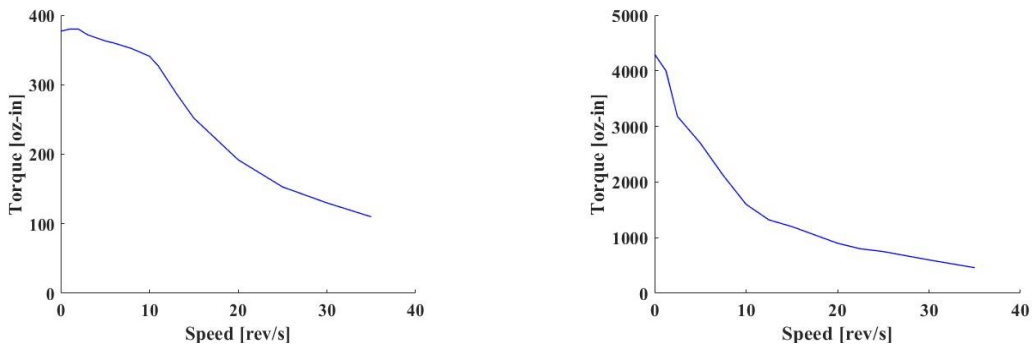

(a) **(b)**

Figure 3-22: Torque curves for (a) vertical motor and (b) lateral motor.

The lateral motion requires rapid and accurate insertion into the plume and therefore requires a dynamic analysis for motor selection. The lateral motion is enabled by a rack and pinion system driven by a stepper motor fastened to four ball-bearing carriages on a double track (Figure 3-24). The rack-and-pinion system allows for both rapid insertion and precise movement once the instrument or article has been inserted into the plume.

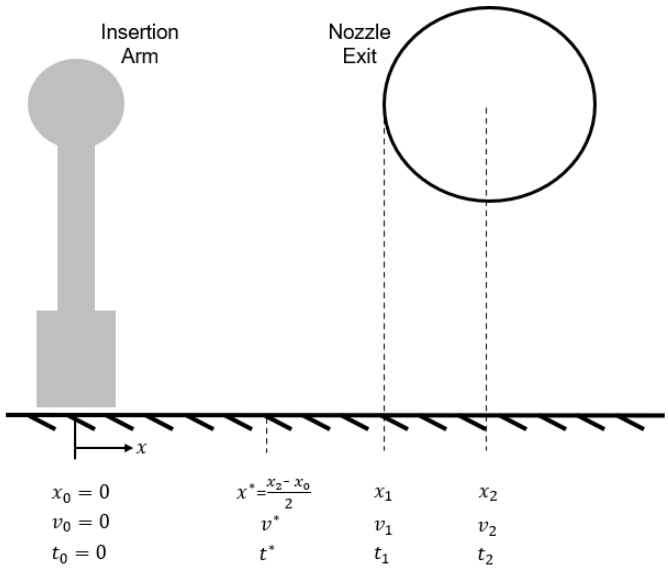

Figure 3-23: Key locations during test article insertion.

A typical insertion profile would accelerate the platform from starting position $x_0 = 0$, then braking the platform at the halfway point $x^* = \frac{x_2 - x_0}{2}$ until it comes to a rest at the nozzle centerline x_2 (key points shown in Figure 3-23). For swept null-point calorimetry, the carriage would accelerate until it reached the edge of the nozzle, x_1, where it would maintain a constant velocity until it reached the opposite side of the nozzle where the carriage would begin to brake to a halt.

The insertion time of the platform, defined as $t_{insertion} = t_2 - t_1$, must be less than 0.25 seconds. Additionally, use of a null-point calorimeter requires a sweep velocity of at least 1 m/s. Therefore, the platform must be able to exceed $v_{null} = 1\ m/s$ at the edge of the nozzle exit x_1. When the carriage reaches x_1, the motor then maintains a constant velocity across the nozzle exit and begins to slow to a halt at the opposite edge of the nozzle exit.

Figure 3-24: Carriage lateral motor during initial assembly.

Because the carriage is constrained in all but the lateral linear motion, the system may be modeled as a system with one linear dimension. The pinion may be modelled as stationary along x while the rack moves along x to simplify the analysis. F_{drive}, the force exerted by the pinion on the rack, is

$$F_{drive} = \tau(\omega)/R \tag{3-10}$$

where R is the pinion radius, $\tau(\omega)$ is the motor torque (taken from the torque curve in Figure 3-22), and ω is the angular velocity of the motor shaft/pinion.

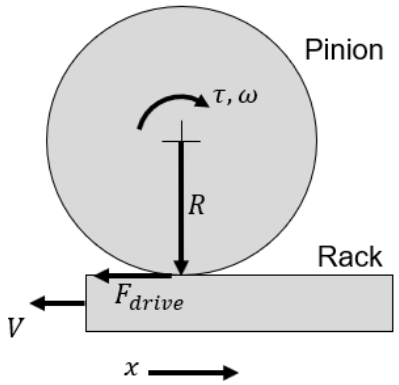

Figure 3-25: Rack and pinion model.

Assuming inertial forces are much greater than friction forces (a reasonable assumption due to the low-friction ball-bearing bogeys which mount the carriage to the rails), friction forces may be neglected. Additionally, the moment of inertia of the pinion and motor shaft is small compared to the carriage inertia. So, the sum of the external forces is

$$\sum F_{ext} = \frac{\tau(\omega)}{R} = m\frac{dV}{dt} \tag{3-11}$$

where m is the mass of the insertion platform, and V is the lateral velocity. This can be rearranged as

$$\frac{dV}{dt} = \frac{\tau(\omega)}{Rm} \tag{3-12}$$

Relating the angular velocity to the linear velocity by

$$V = \omega R \tag{3-13}$$

the torque curve in Figure 3-22 may be reconstructed such that torque is a function of velocity, $\tau(V)$ (Figure 3-26).

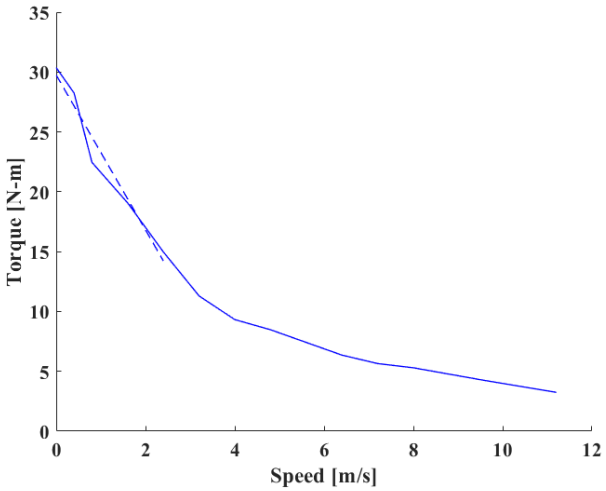

Figure 3-26: Lateral motor torque curve as a function of linear velocity.

Taking a linear fit of the torque curve from 0 m/s to 2.4 m/s (represented by the dashed line in Figure 3-26), the torque as a function of velocity may be approximated as

$$\tau(V) = \alpha V + \beta \tag{3-14}$$

where α and β are constants obtained from the linear fit of the torque curve. (3-12) may then be approximated as

$$\frac{dV}{dt} = AV + B \tag{3-15}$$

where

$$A = \frac{\alpha}{Rm} \tag{3-16}$$

and

$$B = \frac{\beta}{Rm} \tag{3-17}$$

Additionally, because $v = dx/dt$, (3-15) becomes

$$\frac{d^2x}{dt^2} = A\frac{dx}{dt} + B \tag{3-18}$$

Solving (3-15) and (3-18) respectively results in

$$V(t) = c_1 e^{At} - \frac{B}{A} \tag{3-19}$$

and

$$x(t) = \frac{c_1}{A} e^{At} - \frac{B}{A}t + c_2 \tag{3-20}$$

If the carriage starts from rest at initial position $x_0 = 0$ at $t_0 = 0$ (such as during the acceleration phase of test article insertion), then $V(t_0) = 0$ and $x(t_0) = 0$ so

$$c_1 = \frac{B}{A} \tag{3-21}$$

and

$$c_2 = c_1/A \tag{3-22}$$

If the carriage is decelerating from some non-zero velocity V^* at position x^* and time t^* (such as during the braking phase of test article insertion), $V(t - t^* = 0) = V^*$ and $x(t - t^* = 0) = x^*$ so

$$c_1 = V^* + \frac{B}{A} \tag{3-23}$$

and

$$c_2 = x^* - c_1/A \tag{3-24}$$

The solutions to (3-19) and (3-20) were plotted in MATLAB. The predicted position of the carriage with respect to time is plotted in Figure 3-27 and the velocity in Figure 3-28. Additionally, Figure 3-29, shows the lateral velocity as a function of position. In these figures, the solid blue line represents the standard motion profile for inserting a test article

from rest to the centerline of the flow field, while the dashed blue line is the fastest constant velocity sweep for a null-point calorimeter. Note that t_1 and t_2, the time to the nozzle edge and the time to the nozzle centerline respectively, only apply for the standard test article insertion profile, while t_{null} is the time for insertion of a null-point calorimeter during the fastest possible calorimeter sweep at v_{null}.

An Anaheim Motion 42K322 stepper motor was selected based on this model. Video footage of the later tests of the insertion arm confirmed that the actual insertion time closely matched the predicted insertion time, $t_{insertion} = 0.20\ s$. Additionally, the maximum null-point calorimeter velocity is $v_{null} = 2.08\ m/s$, exceeding the original requirements.

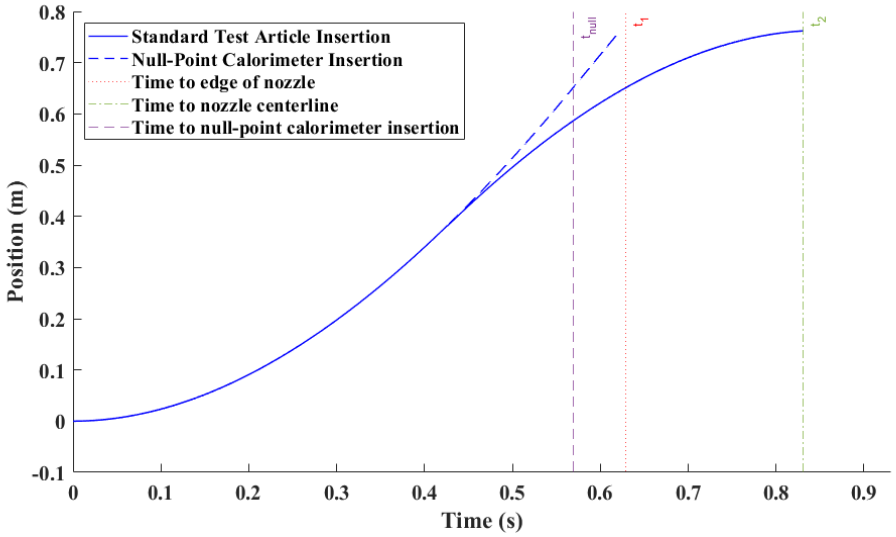

Figure 3-27: Lateral position as a function of time.

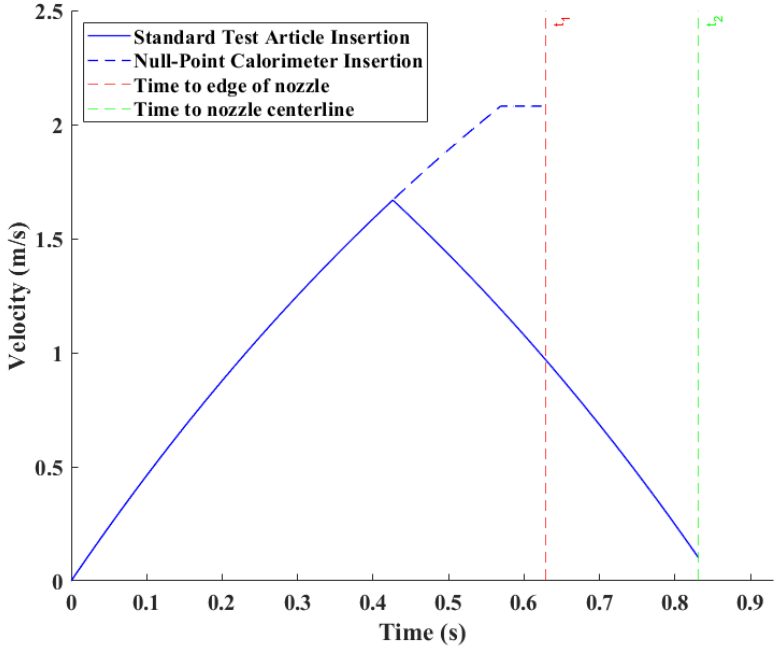

Figure 3-28: Lateral velocity as a function of time.

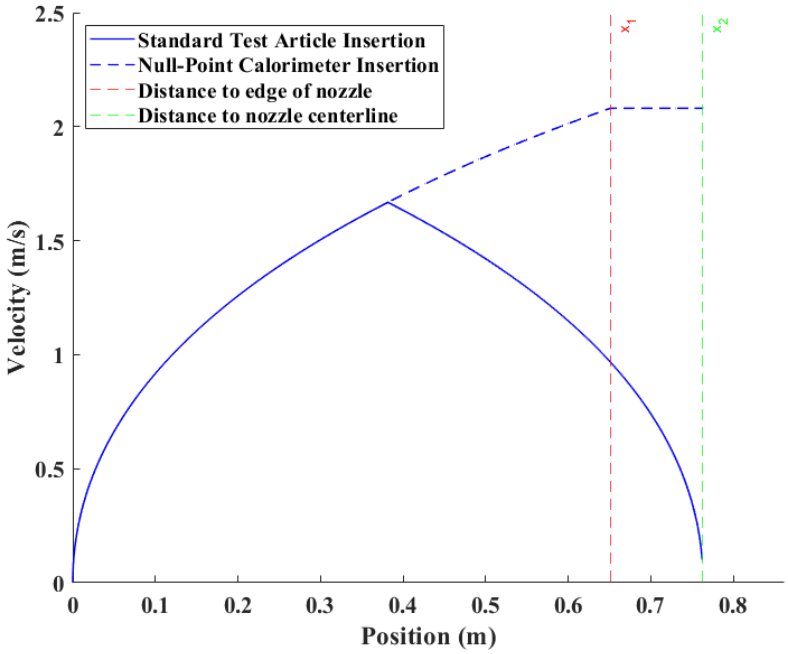

Figure 3-29: Lateral velocity as a function of position.

After the insertion platform was fully assembled and the motors were function tested, a LabView VI was developed to communicate with the insertion platform from a remote computer with an ethernet connection. The LabView control panel includes jogging controls for the vertical motion, jog and motion profile modes for lateral motion, emergency retraction controls, along with temperature, pressure, and coolant flow rate sensors. Additionally, the control panel monitors any intrusive instruments being used during the experiment and collects experimental data.

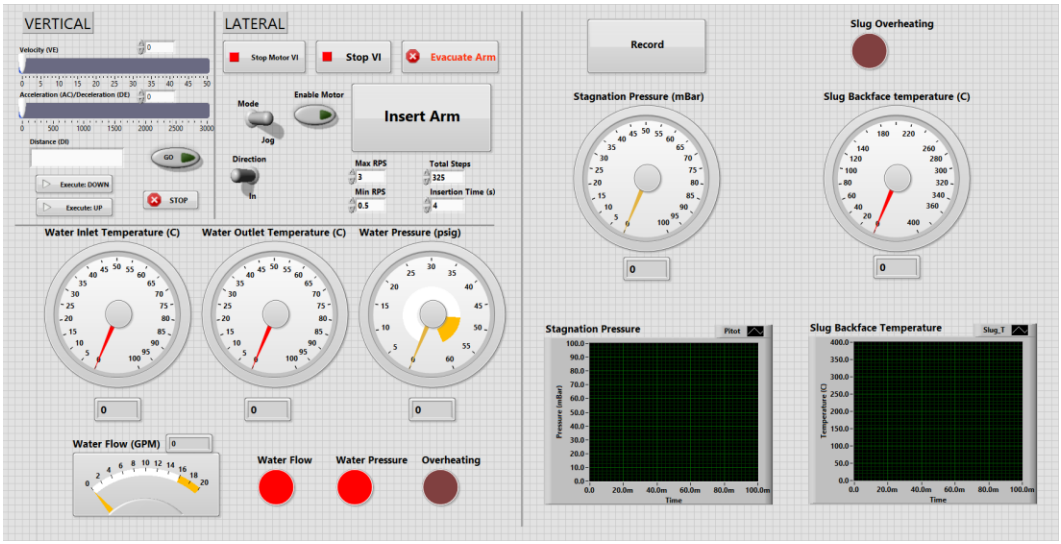

Figure 3-30: Insertion arm control panel with calorimeter.

3.3 Arm Design

Two types of actively cooled intrusive arms were designed to be used in the Mach 4 and Mach 6 flow conditions. These arms were designed to allow for rapid exchange of test articles, and with easy interchangeability between the arms themselves. Both designs use the same 8-hole pattern to mount onto the carriage. Additionally, both arms connect to the same pressurized water system.

Two different designs were developed due to blockage constraints. In the Mach 6 configuration, the larger nozzle exit allows for a larger arm (26% blockage). Conversely, in

the Mach 4 configuration, minimizing blockage effects requires an insertion arm with a small projected area (32% blockage) (Figure 2-31). Additionally, the Mach 4 strut was design with an aerodynamic diamond shape (compared to the cylinder shape of the Mach 6 arm) in order to further minimize the effects of flow blockage.

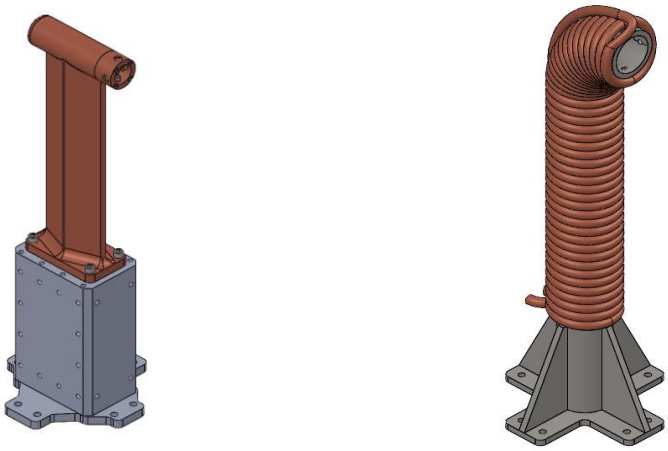

(a) **(b)**

Figure 2-31: a) Mach 4 Insertion Arm. b) Mach 6 Insertion Arm.

3.3.1 Mach 6 Arm

A coiled tube layout was selected for the Mach 6 insertion arm. The core structure was constructed from 1-½ inch Schedule 80 304L stainless steel pipe with a 90◦ elbow welded at one end. Four triangular ribs were welded to the opposite end and a cross-shaped base plate was fastened to the ribs with screws. This core section provides mechanical stiffness to the arm and protects the instrument cables inside from any small amounts of hot gases that may pass through gaps in the copper coil.

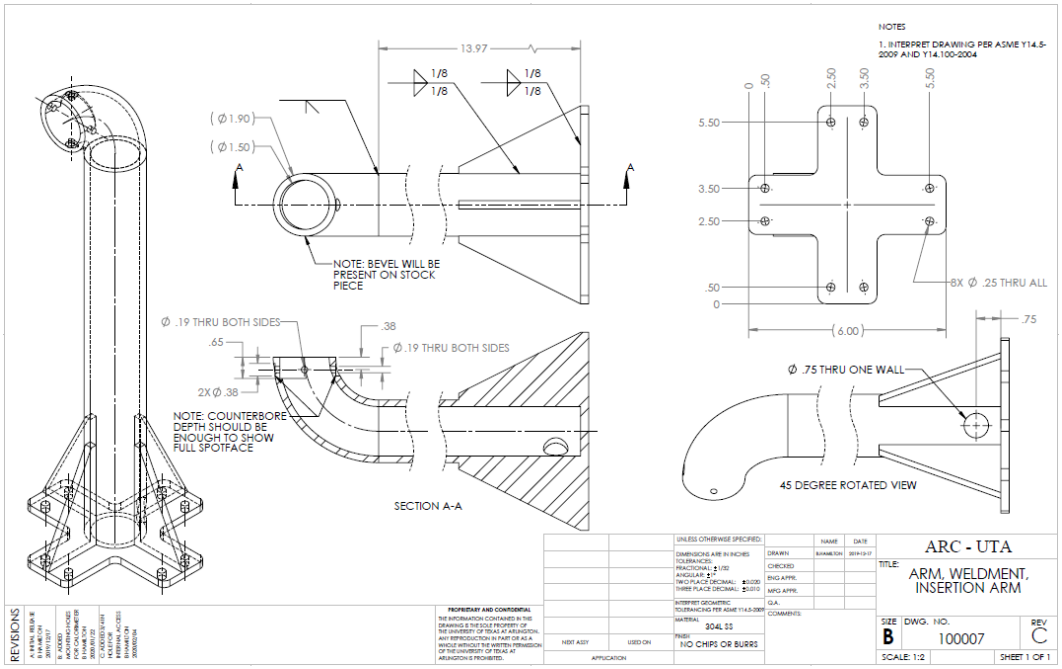

Figure 3-32: Mach 6 arm drawing (without copper tubing wrap).

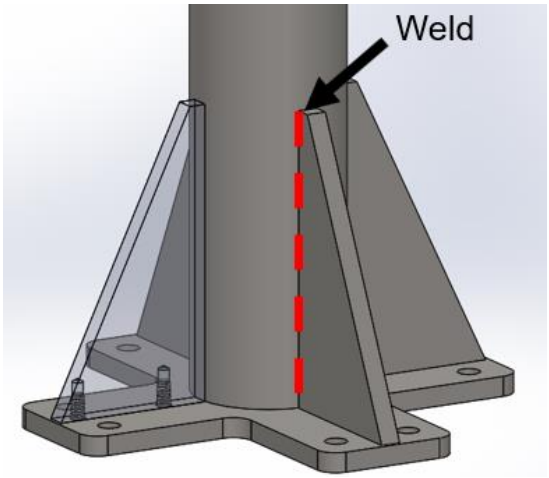

Figure 3-33: Mach 6 arm assembly.

A ¼ inch Type K copper tube was chosen to be used as the external cooling passageway because of its high thermal conductivity and workability, seen in Figure 3-34. The coil was closely wrapped around the pipe in a single layer from bottom to top. A ¼ inch tube was chosen as the largest possible diameter that could be wrapped around the 0.95-inch bending radius of the pipe in order to maximize coolant flow rate.

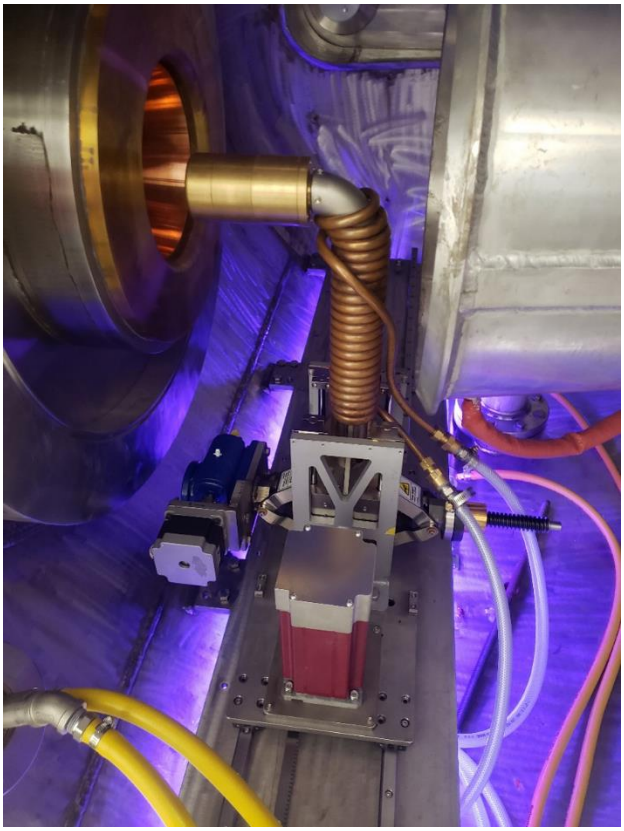

Figure 3-34: Mach 6 arm assembled with external cooling lines.

3.3.2 Mach 4 Arm

For the Mach 4 insertion arm, several previously stated reasons preclude the coiled tube arrangement. The Mach 4 arm was designed as a diamond cross-section with integral cooling passages in the leading and trailing edges (Figure 3-36 and Figure 3-37). The strut was machined out of a single Chromium Copper alloy C18200 billet. Using integral cooling channels provides key benefits. Freed from the external coiled tube bending radius constraints, the cross-sectional area of the cooling channels may be made significantly larger. This increases the flow rate and therefore the cooling power. Additionally, this permitted the design of the aerodynamic blunted diamond shape shown in Figure 2-6, which serves to reduce the effects of blockage in the arc-jet. To reduce the

effects of local heating away from the cooling channels, the entire arm was chosen to be constructed from high thermal conductivity copper.

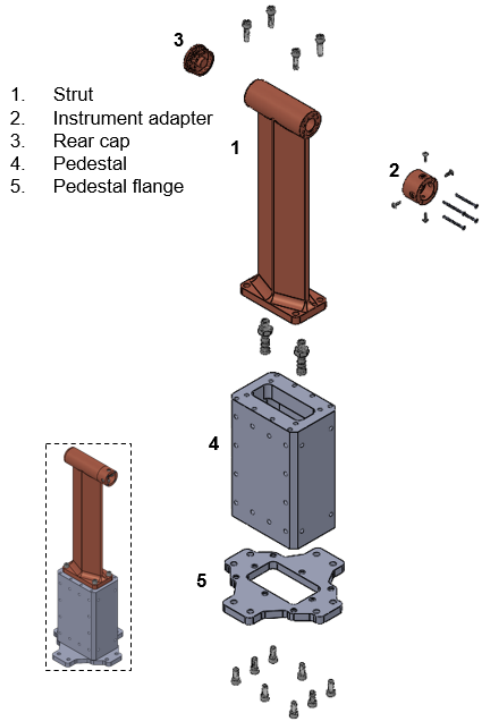

Figure 3-35: Mach 4 arm exploded view.

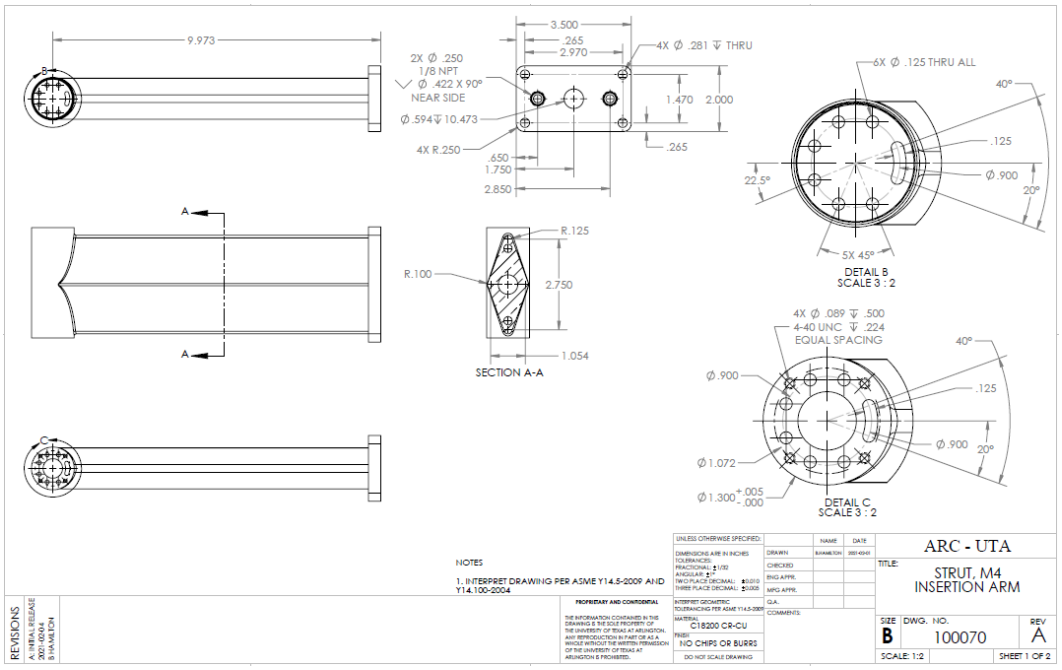

Figure 3-36: Mach 4 arm strut drawing.

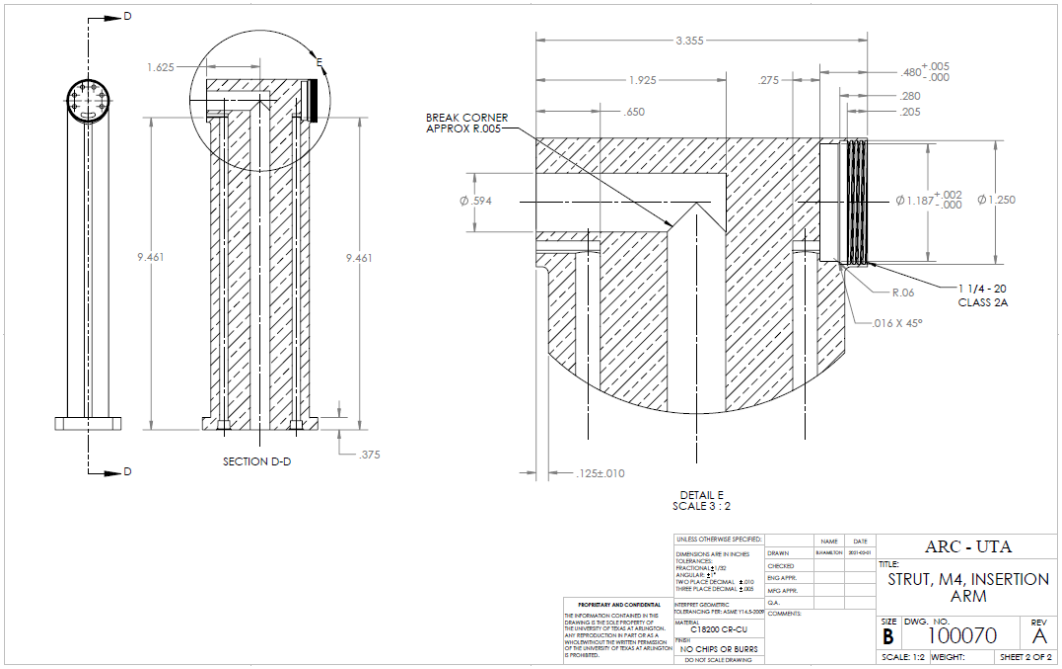

Figure 3-37: Mach 4 arm strut drawing detail.

Additional components for the Mach 4 arm include an instrument adapter (Figure 3-38) and a rear cap (Figure 3-39). The instrument adapter functions as a flow containment device for the strut cooling channels, as well as providing a mounting point for test articles using a 4-hole radial pattern. It attaches to the strut using four screws in the axial direction. Due to the compound curves in the instrument adapter, silicone gasket material is manually applied along the perimeter to seal the cooling channels.

The rear cap, being a revolved shape, is simpler. It attaches to the strut with a single thread and utilizes an o-ring seal.

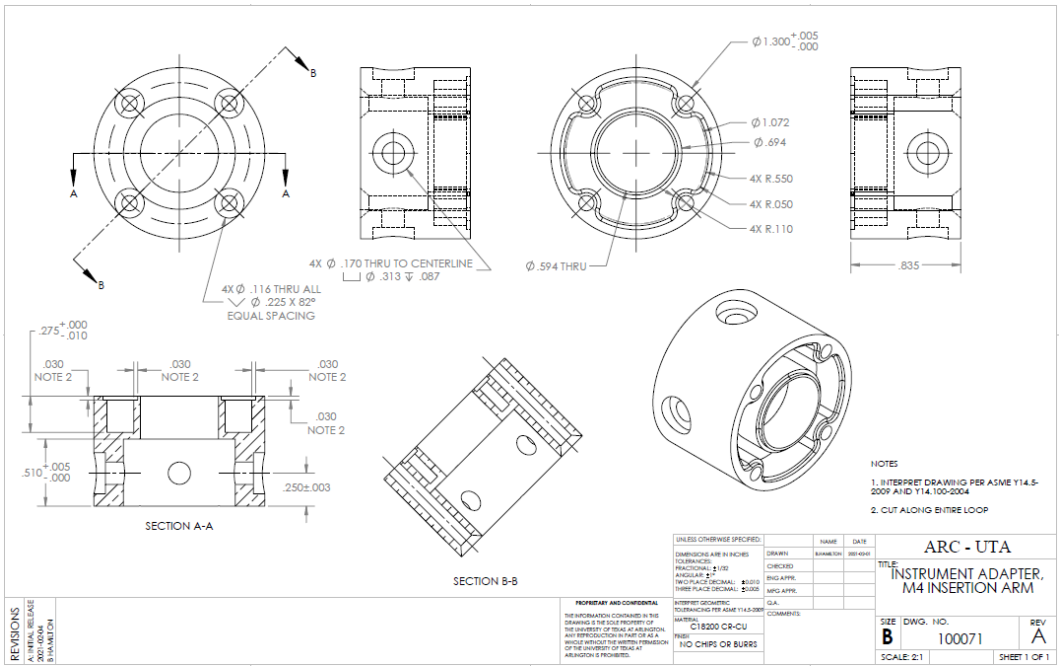

Figure 3-38: Mach 4 arm instrument adapter drawing.

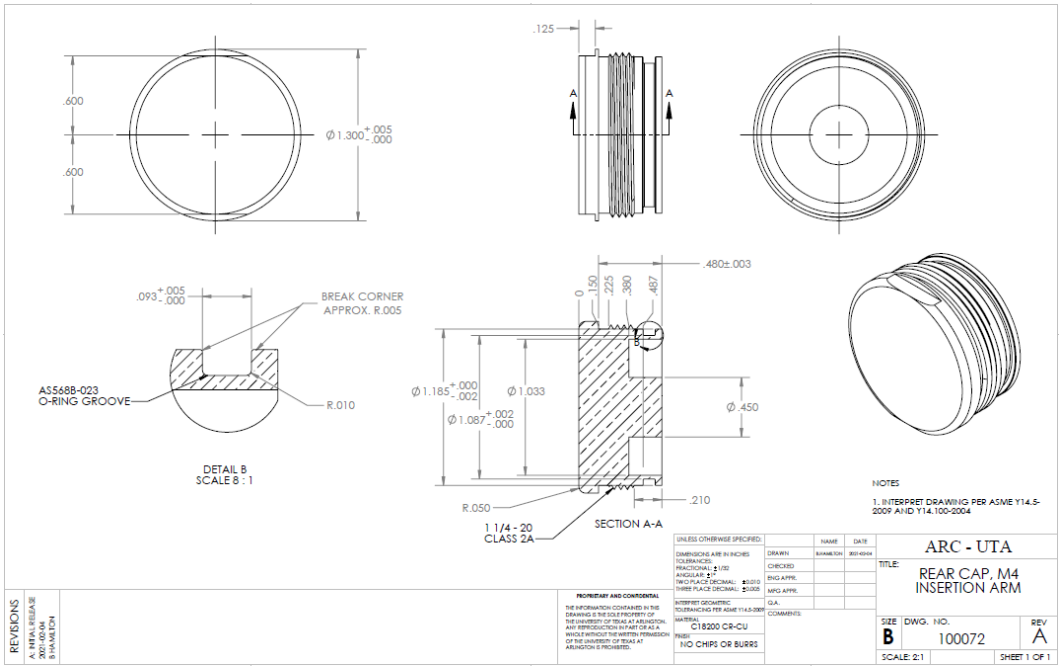

Figure 3-39: Mach 4 arm rear cap drawing.

The downside of using integrated cooling channels in the arm is manufacturing difficulties. The strut and instrument holder needs to be manufactured as one large piece, with channels drilled through its length. Therefore, the arm needed to be made shorter in order to allow it to fit in a CNC mill. Fortunately, because the plume of the Mach 4 nozzle is significantly smaller in diameter, a shorter length of the actively cooled portion of the strut is acceptable. An uncooled, 6061 aluminum pedestal (Figure 3-40) was developed which serves to elevate the top of the shorter Mach 4 insertion arm up to the centerline of the nozzle. Additionally, this component serves as a housing for the insertion arm's cooling fluid connections. This pedestal is located well outside the zone of direct flow impingement to minimize heat transfer. It then attaches to the carriage flange adapter using the same 8-hole pattern at the Mach 6 arm (Figure 3-41).

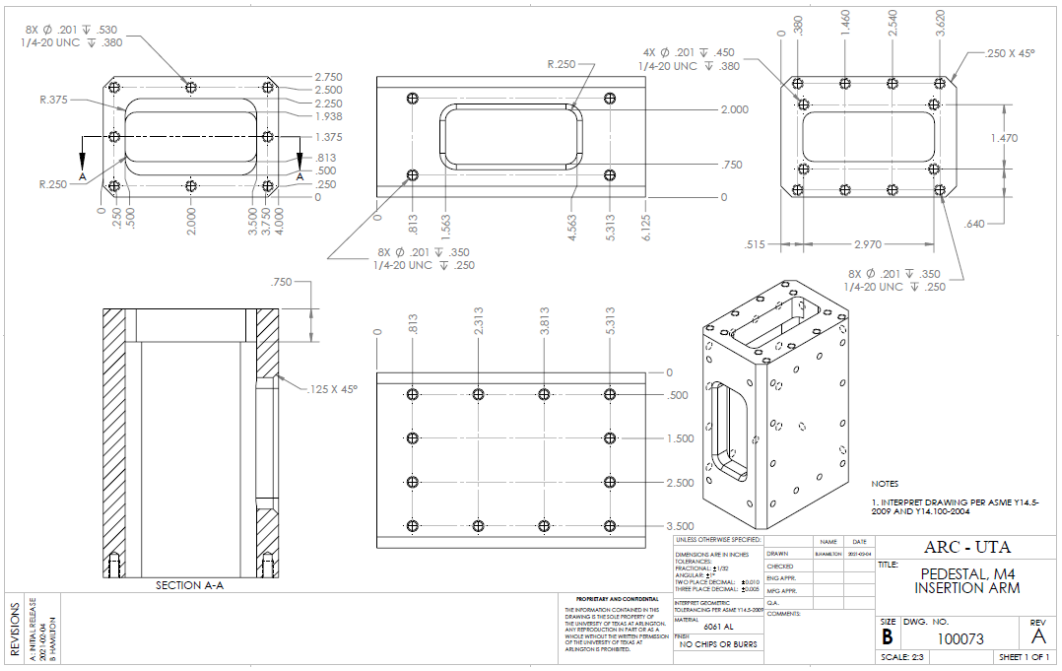

Figure 3-40: Mach 4 arm pedestal drawing.

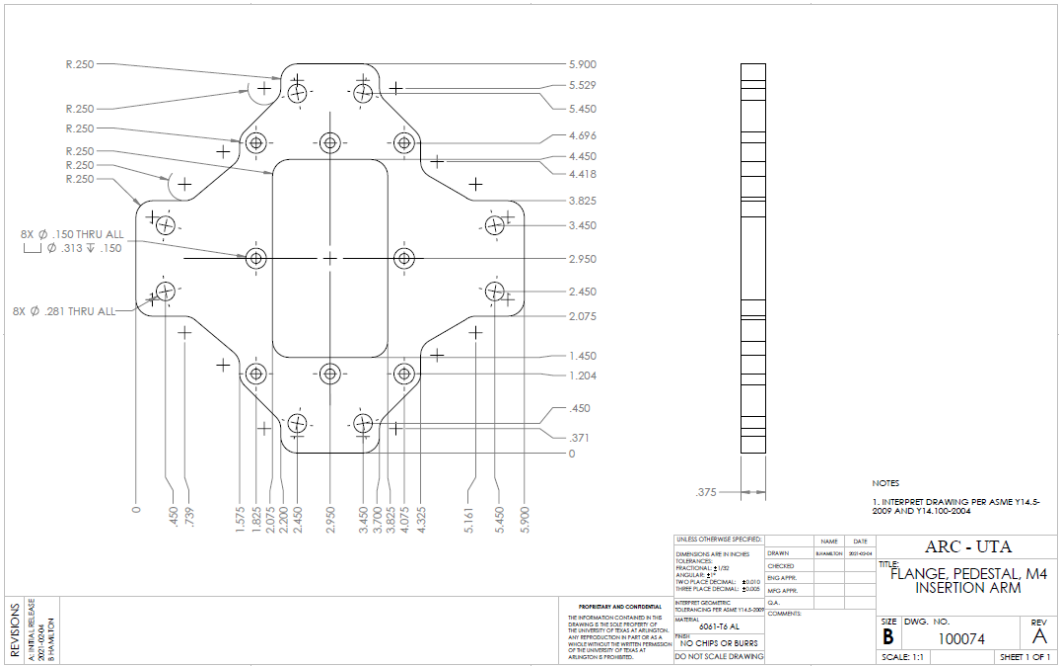

Figure 3-41: Mach 4 arm pedestal flange drawing.

3.3.3 Mach 4 Arm Double Mount

(a) **(b)**

Figure 3-42: (a) CAD model of double arm and (b) installed double arm.

In order to expand the capabilities of the insertion system, a double arm pedestal was developed and constructed (Figure 3-42). With the double pedestal, two test articles may now be inserted during a single arc-jet run. By applying a 20° half-angle between two arms (seen in Figure 3-43), an 8.2-inch gap between the centerlines of each instrument is attained on the same carriage.

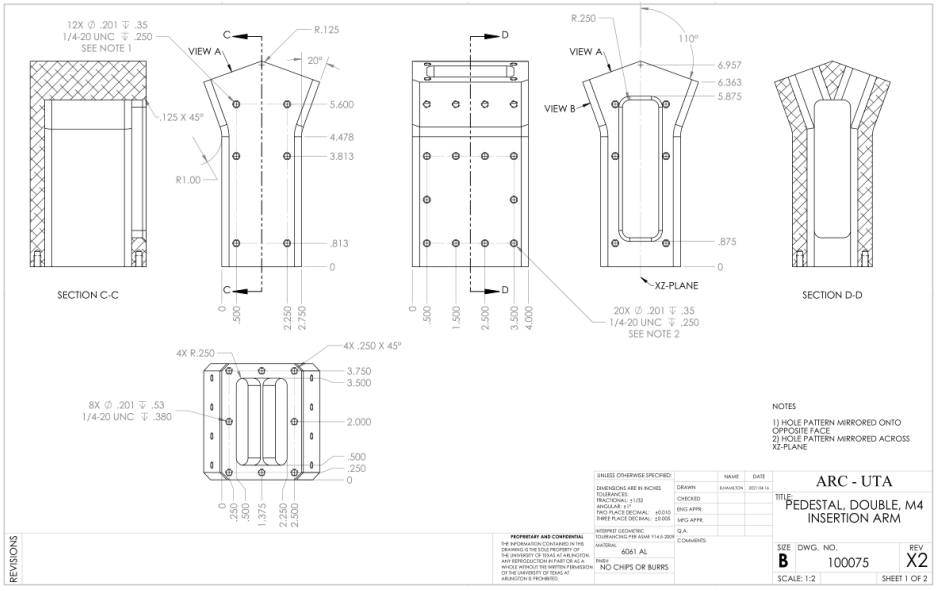

Figure 3-43: Double arm pedestal drawing.

3.4 Other Components

3.4.1 Instruments

By the modular nature of this platform's design, various intrusive instruments can be utilized to assist in characterization of the arc-jet flow field. Current instruments include in-house developed slug-type calorimeters [23] for both the Mach 4 and 6 nozzle configurations and a 20° half-angle wedge for shear flow measurements for Mach 4. Additionally, a null-point calorimeter, TPS holder, and Mach 6 wedge are under development. A selection of these test articles is shown in Figure 3-44. Additionally, a double-arm fixture has been designed allowing for more than one test article to be used during a single run (Figure 3-42).

(a) **(b)**

Figure 3-44: Slug-calorimeter, TPS material holder, and shear wedge for (a) Mach 4 conditions and (b) Mach 6 conditions.

3.4.2 Alignment Tools

In order to ensure proper alignment of the test article to the flow centerline during insertion, alignment tools were developed. The Mach 6 alignment tool (Figure 3-45) is a composed primarily of a revolved housing that matches the cone angle of the nozzle is order to ensure that the tool's axis of revolution matches the flow centerline axis. The housing is constructed from acetal thermoplastic due to ease of machining and low friction

to avoid sticking in the nozzle. Inside the housing, a cavity is machined that approximately matches the standard dimensions of a 12-gauge shotgun chamber [24] in order to allow the installation of an off-the-shelf shotgun lase boresight tool. Then, two handles are attached to ease insertion and removal of the tool. The laser, aligned to the centerline, may then be used to quickly located the desired location of the flow centerline on the test article to be inserted.

The Mach 4 alignment tool is broadly similar, except smaller in diameter to match the smaller Mach 4 nozzle.

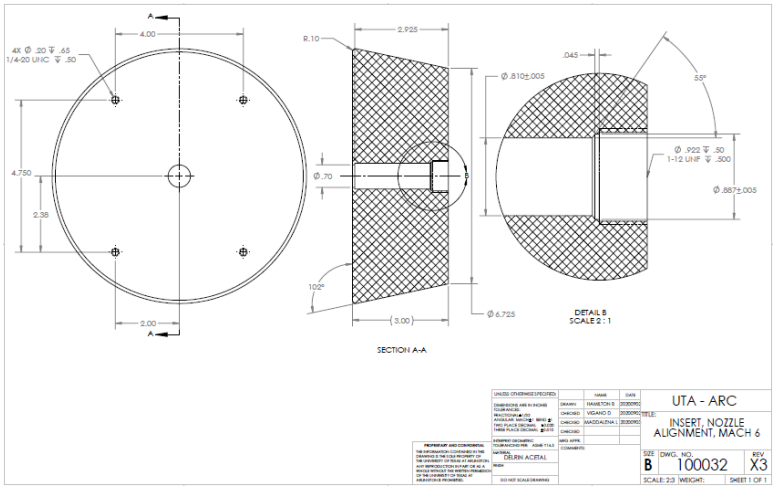

(a)

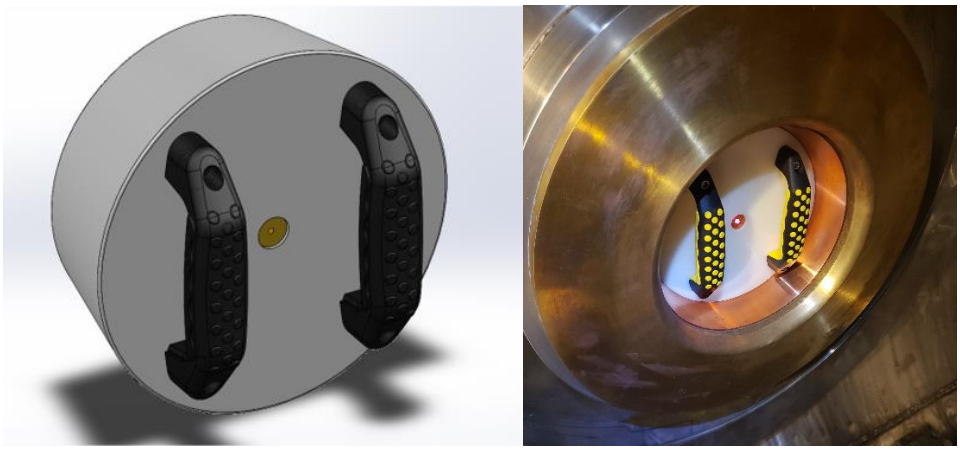

(b) (c)

Figure 3-45: (a) Mach 6 alignment tool drawing, (b) Mach 6 alignment tool CAD assembly, and (c) Mach 6 alignment tool constructed and in use.

3.5 Testing and Results

The Mach 6 design was operated successfully for the first time during an AHWT run in October 2020, in June 2021, the Mach 4 design operated successfully as well (Figure 3-46). A thorough post-firing inspection showed no mechanical failures or scorching on the exposed surfaces (Figure 3-47).

Measurements of the inlet and outlet water temperatures for the Mach 6 runs were taken (Figure 3-48 and Figure 3-49), with a maximum measured ΔT of 2.2 K and 6.1 K respectively. A plot of cooling power versus time was created using (2-36). However, unexpected flow separation in the Mach 6 runs caused a narrower plume, making comparison Figure 2-7 difficult. Nevertheless, the cooling system functioned well and prevented damage during these conditions.

Measurements of the inlet and outlet water temperatures for the Mach 4 run were taken (Figure 3-50), with a maximum measured ΔT of 8.5 K . A plot of cooling power versus time was created using (2-36) (also shown in Figure 3-50). Although the arm did not reach its steady state cooling limits, the temperature difference and cooling power are well within the expected values in Figure 2-7.

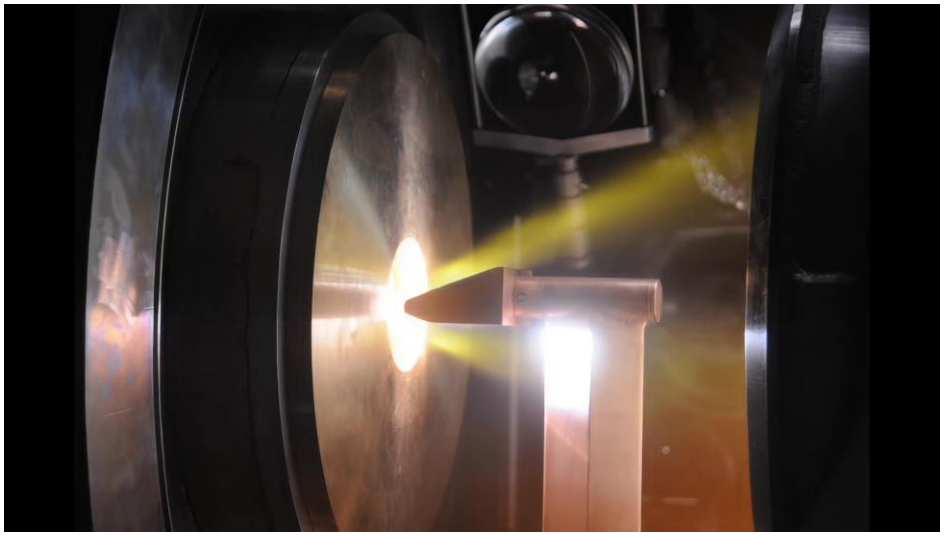

Figure 3-46: Mach 4 wedge during testing with shear wedge taking direct measurements of shear stress.

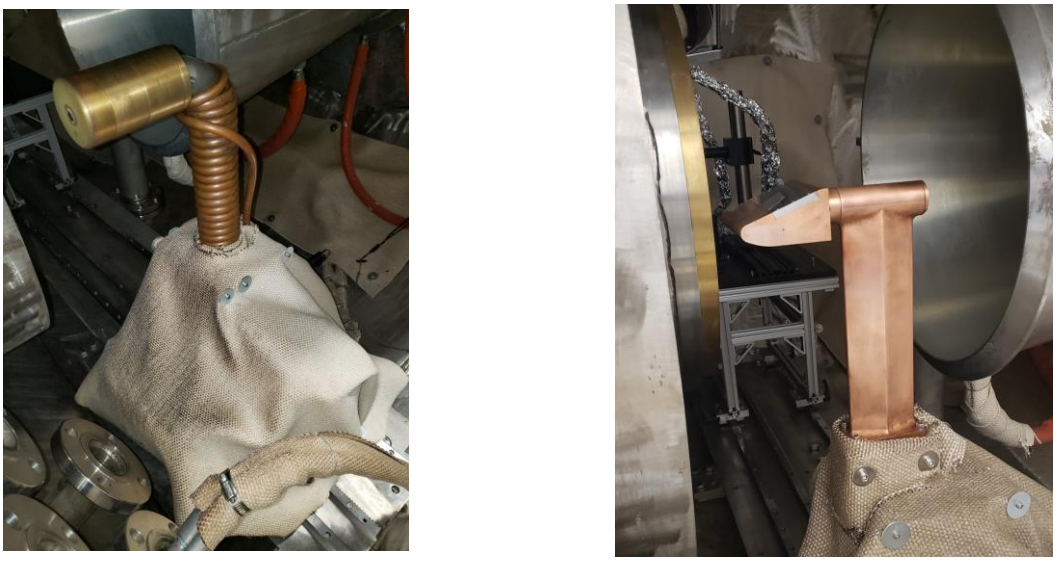

(a) **(b)**

Figure 3-47: (a) Mach 6 arm and calorimeter after testing and (b) Mach 4 arm and shear wedge after testing.

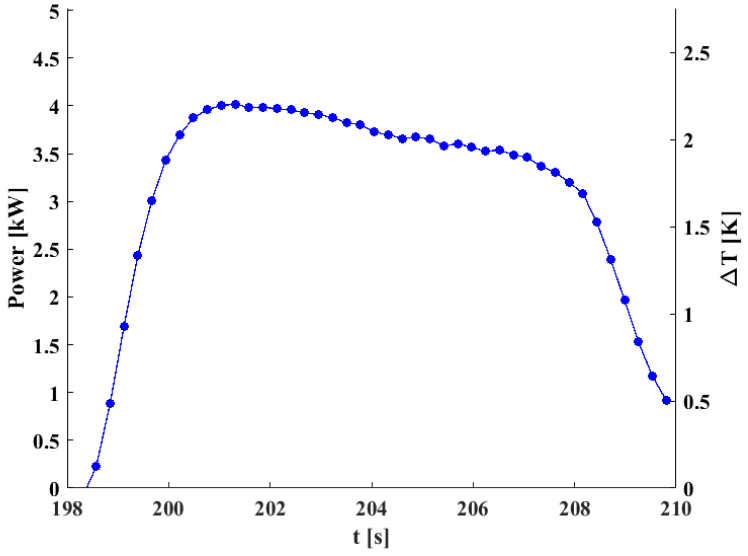

Figure 3-48: Mach 6 insertion arm experimentally measured cooling power vs time (first run).

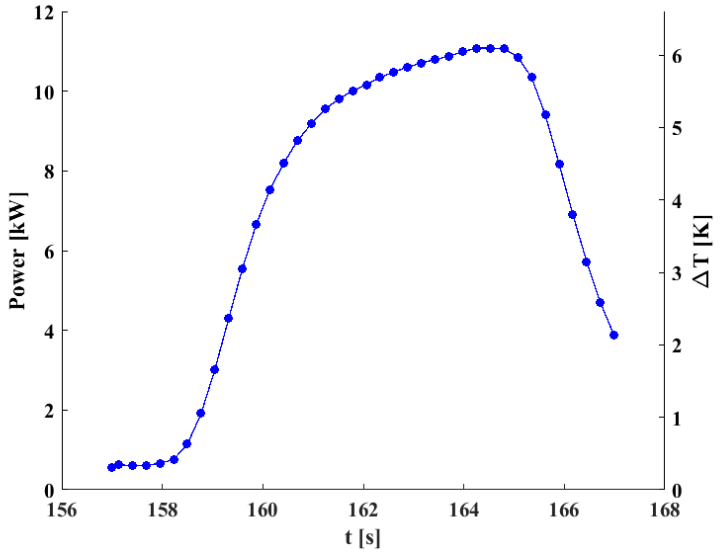

Figure 3-49: Mach 6 insertion arm experimentally measured cooling power vs time (second run).

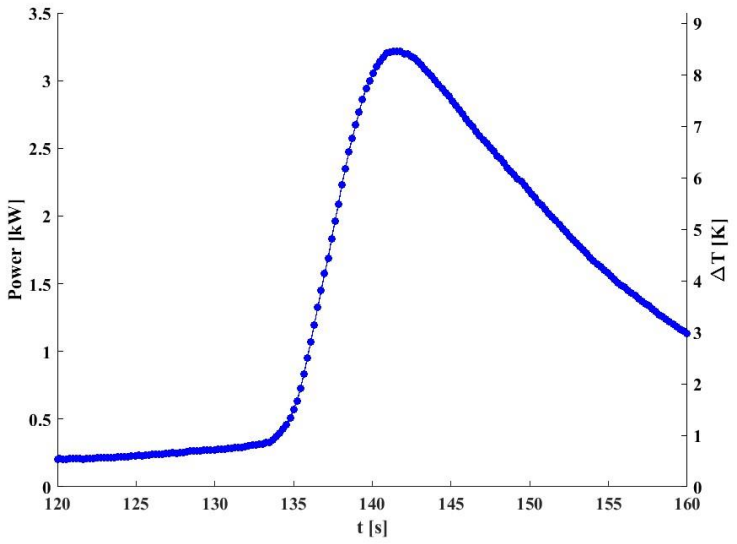

Figure 3-50: Mach 4 insertion arm experimentally measured cooling power vs time.

Chapter 4

4.1 Conclusions

The design approach for a modular platform for intrusive diagnostics and TPS testing, along with its successful operation, has been presented. The final design consists of a carriage which includes the active motion components of the platform, and the insertion arms which contain the active-cooling components of the design.

Focus has been placed on analysis of the thermal loads and the performance of the active cooling system. Equations from Fay-Riddell and Zoby were used to determine stagnation point heating. Then, a scaled heat flux profile method and the reference temperature method were used to determine local heating on the Mach 4 arm. Additionally, the aerodynamic loads and the deflection responses were determined for each arm using simplified analysis methods, including a modified shock-expansion analysis.

Two insertion arms have been designed for different flow conditions, each with different geometry. Due to less stringent blockage and thermal constraints, the Mach 6 arm is a simpler design with external wrapped cooling passages. Conversely, the Mach 4 arm is a more complex design with compact integrated cooling passages. Additionally, a double mount for the Mach 4 arm has been developed which allows for multiple test articles to be deployed.

The motor selection process was also presented. Selection of the motor for the vertical motion employed a simple energy balance method. For the lateral motion, a rigid body model was used to predict the motion profile in order to select a motor to rapidly insert the arm into the high-enthalpy flow in a sufficiently short time frame.

Both Mach 4 and Mach 6 insertion arms have been successfully tested. Experimental observations in the Mach 4 high-enthalpy flow show a maximum temperature

difference between the inlet and outlet of the cooling system of 8.5 K, and peak temperature difference of 6.1 K in the Mach 6 arm cooling system..

4.2 Future Work

Further improvements to the insertion platform are being developed. This includes developing additional instrumentation to increase diagnostic capabilities, a closed-loop positioning system for the lateral motor, a double instrument holder, and other miscellaneous improvements to the platform to ease construction/maintenance and improve performance.

In order to allow for multiple test articles to be inserted into the plume during a single arc-jet run, a double instrument mount is being developed (Figure 4-1). Although uncooled, this attachment will utilize copper heat sinks to allow short insertion times. This design will be further adapted in the future to include active cooling along the leading edge.

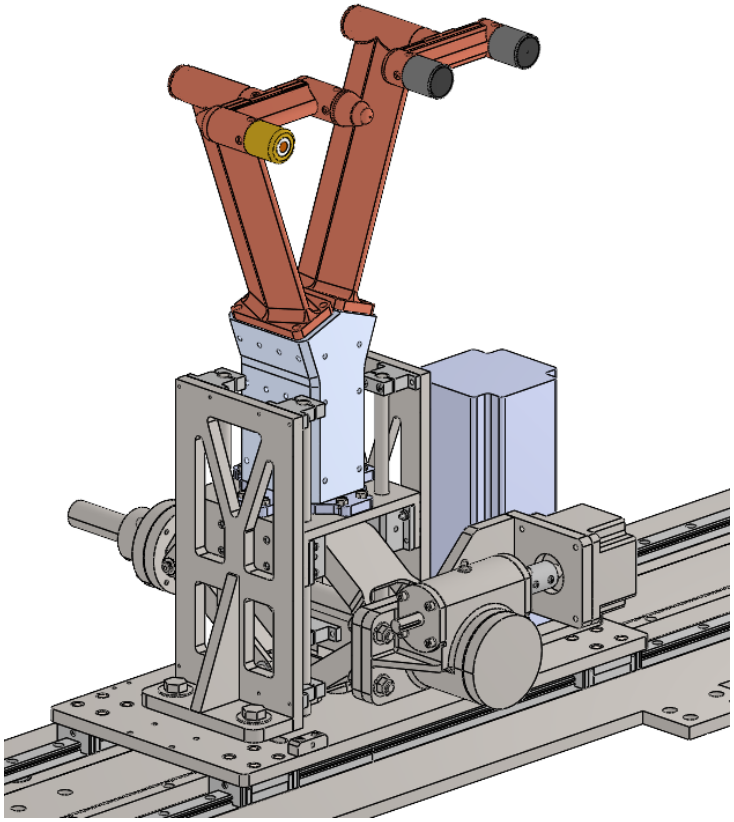

Figure 4-1: Insertion platform CAD model with multiple arms and test articles mounted.

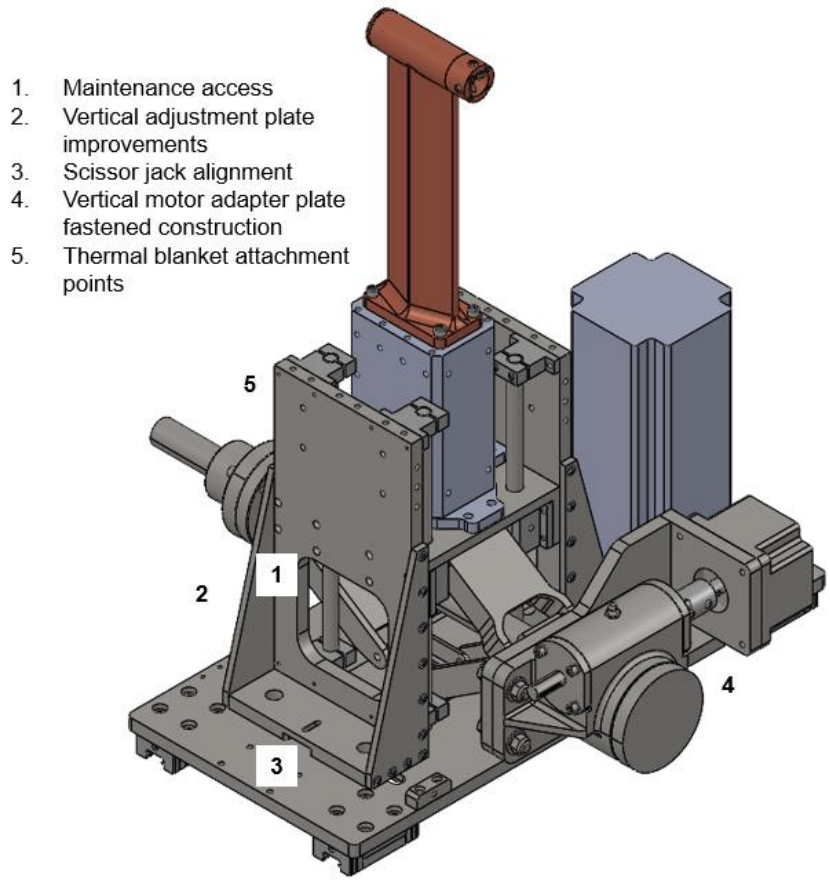

Figure 4-2: Carriage design improvements

Although the as-built carriage performs adequately, several ways to improve the maintenance and operation of the carriage have been identified (Figure 4-2). The vertical adjustment plates have been completely redesigned. The triangular rib in the center has been replaced by two ribs fastened to the outside of the plate. This allows for the creation of a large opening to ease assembly/disassembly and maintenance of the scissor jack. Access holes for the guide rail bearing housings have also been included, further easing access. The bottom of the vertical adjustment plate has also been modified to include a lateral slot, which allows fine-tuning of the base location of the scissor jack. Additionally,

several tapped holes are included around the edges of the vertical adjustment plates to ease the installation of thermal blankets or other thermal protection materials.

In the new design, fasteners are used in lieu of welds for all parts. Changing to fasteners over welds eliminates struggles that emerged from the welded design, particularly warping in the vertical adjustment plates which caused difficulties aligning the vertical guide rails.

Appendix A

Lateral motion MATLAB code

```
clear all
close all
clc

M = 120;        % cart mass, kg
R = 0.05093;    % pinion radius, m
D_noz = 8.75*0.0254;   % nozzle diameter, m.
R_noz = D_noz/2;
x_2 = 30*0.0254;     % distance to nozzle, m
x_star = x_2/2;
x_1 = (x_2 - R_noz); %distance to nozzle exit edge, m
alpha = -6.468;
beta = 29.747;
A = alpha/(R*M);
B = beta/(R*M);
c1 = B/A;
c2 = -B/(A^2);

xfit = [0 2.4];
yfit = alpha.*xfit + beta;

%input torque curve
Tauozin = [4300 4000 3180 2700 2120 1600 1320 1200 1050 900 800
750 600 460];   % [oz-in]  Torque
rps =     [0    1.25 2.5  5    7.5  10   12.5 15   17.5 20  22.5
25  30  35  ]; % [rps] Speed
TauNm    = Tauozin.*0.00706155183;   % [Nm]  Torque
MotorSpeed    = rps.*2.*pi.*R;      %  Speed, m/s

deltat = 0.001;  %time step, s
t_max = 3;  % max time for first half, s
%tau = 19;  %torque, N-m
i = 1;
j = 1;
k = 1;
h = 1;

%first half of profile
ta = (0:deltat:t_max);  %time, s
xa = zeros(length(ta),1);  %position, m
va = zeros(length(ta),1);   %velocity, m/s

%second half of profile
tb = (0:deltat:t_max);
```

```
xb = zeros(length(tb),1);
vb = zeros(length(tb),1);

%null point calorimeter profile
tnull = (0:deltat:t_max);
xnull = zeros(length(tnull),1);
vnull = zeros(length(tnull),1);

%first half of insertion profile
while xa(i)<x_star
    va(i) = c1*exp(A*ta(i)) - B/A;
    xa(i) = (c1/A)*exp(A*ta(i)) - (B/A)*ta(i) + c2;
    if xa(i)>x_star && j == 1
       v_star = va(i)
       t_star = ta(i);
       i_star = i;
       j = 2;
       i = i + 1;
       break
    end
    i = i + 1;
end

%null point calorimeter profile
while xnull(k)<x_1
    vnull(k) = c1*exp(A*tnull(k)) - B/A;
    xnull(k) = (c1/A)*exp(A*tnull(k)) - (B/A)*tnull(k) + c2;
    if xnull(k)>x_1 && h == 1
       v_nullmax = vnull(k)
       x_nullmax = xnull(k);
       t_nullmax = tnull(k);
       h = 2;
       k = k+1;
       break
    end
    k = k + 1;
end
while xnull(k)<x_2
    vnull(k) = v_nullmax;
    xnull(k) = x_nullmax + vnull(k).*(tnull(k)-t_nullmax);
    if xnull(k)>x_2 && h == 2
       h = 3;
       break
    end
    k = k + 1;
end

xnull((k+1):length(tnull))=[];
xnull(1:i)=[];
vnull((k+1):length(tnull))=[];
```

```
vnull(1:i)=[];
tnull((k+1):length(tnull))=[];
tnull(1:i)=[];
k = 1;

alpha = 6.468;
beta = -29.747;
A = alpha/(R*M);
B = beta/(R*M);
c1 = (v_star + B/A);
c2 = x_star - c1/A;

% second half of insertion profile
while xb(k)<x_2
    vb(k) = c1*exp(A*tb(k)) - B/A;
    xb(k) = (c1/A)*exp(A*tb(k)) - (B/A)*tb(k) + c2;
    if xb(k)>x_1 && j == 2
       v_1 = vb(k);
       t_1 = tb(k)+t_star;
       k_1 = k;
       j = 3;
    end
    if xb(k)>x_2 && j == 3
       t_2 = tb(k)+t_star;
       k_2 = k;
       j = 4;
       break
    end
    k = k + 1;
end

xa((i):length(ta))=[];
va((i):length(ta))=[];
ta((i):length(ta))=[];

xb((k+1):length(tb))=[];
vb((k+1):length(tb))=[];
tb((k+1):length(tb))=[];

vc = [va; vb];
xc = [xa; (xb)];
tc = [ta, (tb+t_star)];

t_insertion = t_2-t_1

figure(1)
hold on
plot(tc,vc,'-b','MarkerFaceColor','b','linewidth',1)
plot(tnull,vnull,'--b','MarkerFaceColor','b','linewidth',1)
```

```
set(gca,'fontsize',16,'fontname','Times New
Roman','fontweight','bold');
xlabel('Time (s)')
ylabel('Velocity (m/s)')
xline(t_1, ':', 't_1','Color','red');
xline(t_2, '-.', 't_2','Color','#77AC30');
xline(t_nullmax, '--', 't_n_u_l_l','color','#7E2F8E');
xlim([0 t_2+.1])
legend('Standard Test Article Insertion', 'Null-Point Calorimeter
Insertion', 'Time to edge of nozzle', 'Time to nozzle
centerline','Time to null-point calorimeter
insertion','Location','northwest')

figure(2)
hold on
plot(tc,xc,'-b','MarkerFaceColor','b','linewidth',1)
plot(tnull,xnull,'--b','MarkerFaceColor','b','linewidth',1)
set(gca,'fontsize',16,'fontname','Times New
Roman','fontweight','bold');
xlabel('Time (s)')
ylabel('Position (m)')
xline(t_1, ':', 't_1','Color','red');
xline(t_2, '-.', 't_2','Color','#77AC30');
xline(t_nullmax, '--', 't_n_u_l_l','color','#7E2F8E');
xlim([0 t_2+.1])
legend('Standard Test Article Insertion', 'Null-Point Calorimeter
Insertion', 'Time to edge of nozzle', 'Time to nozzle
centerline','Time to null-point calorimeter
insertion','Location','northwest')

figure(3)
hold on
plot(xc,vc,'-b','MarkerFaceColor','b','linewidth',1)
plot(xnull,vnull,'--b','MarkerFaceColor','b','linewidth',1)
set(gca,'fontsize',16,'fontname','Times New
Roman','fontweight','bold');
xlabel('Position (m)')
ylabel('Velocity (m/s)')
xline(x_1, ':', 'x_1','Color','red');
xline(x_2, '-.', 'x_2','Color','#77AC30');
yline(v_nullmax, '--', 'v_n_u_l_l','color','#7E2F8E');
xlim([0 t_2+.1])
ylim([0 v_nullmax+1])
legend('Standard Test Article Insertion', 'Null-Point Calorimeter
Insertion', 'Distance to edge of nozzle', 'Distance to nozzle
centerline','Maximum null-point calorimeter
velocity','Location','northwest')

figure(4)
hold on
```

```
plot(MotorSpeed,TauNm,'-b','MarkerFaceColor','b','linewidth',1)
plot(xfit,yfit,'--b','MarkerFaceColor','b','linewidth',1)
set(gca,'fontsize',16,'fontname','Times New
Roman','fontweight','bold');
xlabel('Speed [m/s]')
ylabel('Torque [N-m]')
```

References

[1] Nawaz, A., Gorbunov, S., Terrazas-Salinas, I., and Jones, S., “Investigation of slug calorimeter gap influence for plasma stream characterization,” *43rd AIAA Thermophysics Conference*, 2012, p. 3186.

[2] Hammock, G., “Design and Calibration of the AEDC H3 Mach 3.0 High Heat Flux Nozzle,” *30th AIAA Aerodynamic Measurement Technology and Ground Testing Conference*, 2014, p. 2653.

[3] Gokcen, T., and Alunni, A., “Flow Characterization Studies of the 10-MW TP3 Arc-Jet Facility: Probe Sweeps,” *46th AIAA Thermophysics Conference*, 2016, p. 4153.

[4] Scott, C., Suess, L., Milhoan, J., Oelke, L., Godfrey, D., Larin, M., Grinstead, J., and Del Papa, S., “Enthalpy Distributions of Arc Jet Flow Based on Measured Laser Induced Fluorescence, and Heat Flux and Stagnation Pressure Distributions,” *42nd AIAA Thermophysics Conference*, 2011, p. 3778.

[5] Esser, B., Koch, U., and Gülhan, A., “Results of the Experimental Study in the L2K Facility,” 2011.

[6] Park, C., Raiche, G. A., Driver, D. M., Olejniczak, J., Terrazas-Salinas, I., Hightower, T. M., and Sakai, T., “Comparison of enthalpy determination methods for an arc-jet facility,” *Journal of thermophysics and heat transfer*, Vol. 20, No. 4, 2006, pp. 672–679.

[7] Purpura, C., et al. "Experimental characterisation of the CIRA plasma wind tunnel SCIROCCO test section." *Acta Astronautica* 62.6-7 (2008): 410-421.

[8] Terrazas-Salinas, Imelda, and C. Cornelison. "Test Planning Guide for NASA Ames Research Center Arc Jet Complex and Range Complex." *Space*

Technology Division, NASA Ames Research Center, Moffett Field, CA 94035 (2009): 20-21.

[9] Lu, Frank K., and Dan E. Marren. Advanced Hypersonic Test Facilities. Reston, Va: *American Institute of Aeronautics and Astronautics*, 2002. Print.

[10] Ronciglia, Giuseppe. “Tecniche Innovative Sulla Taratura Di Pressioni Assolute e Relative.” Blog WIKA, 24 June 2019, https://blog.wika.it/wika-insight/tecniche-innovative-sulla-taratura-di-pressioni-assolute-e-relative/.

[11] “High-Enthalpy Arc-Heated Facilities at AEDC.” Arnold Air Force Base, 16 Jan. 2013, https://www.arnold.af.mil/About-Us/Fact-Sheets/Display/Article/409285/high-enthalpy-arc-heated-facilities-at-aedc/.

[12] Campbell, David Ray. *Conjugate Heat Transfer and Thermo-Structural Analysis of the Actively Cooled Multi-Stage Conical Nozzle and Hypersonic Low-Reynolds Diffuser of the New Arc-Heated Wind Tunnel (AWHT-II) of the University of Texas at Arlington*. Diss. 2017.

[13] Standard Test Method for Measuring Extreme Heat-Transfer Rates from High Energy Environments Using a Transient, Null-Point Calorimeter. 2008th ed. West Conshohocken, PA: American Society Testing & Materials ASTM, 2009. Print.

[14] Löhle, Stefan, et al. "Improvement of high heat flux measurement using a null-point calorimeter." *Journal of Spacecraft and Rockets* 45.1 (2008): 76-81.

[15] Fay, J. A., and Riddell, F. R., “Theory of stagnation point heat transfer in dissociated air,” *Journal of the Aerospace Sciences*, Vol. 25, No. 2, 1958, pp. 73–85.

[16] Anderson, J. D., *Hypersonic and High Temperature Gas Dynamics*, AIAA, 2000.

[17] Zoby, E. V., *Empirical stagnation-point heat-transfer relation in several gas mixtures at high enthalpy levels*, Vol. 4799, National Aeronautics and Space Administration, 1968.

[18] Zoby, E. V., and Sullivan, E. M., “Effects of corner radius on stagnation-point velocity gradients on blunt axisymmetric bodies,” *Journal of Spacecraft and Rockets,* Vol. 3, No. 10, 1966, pp. 1567–1567.

[19] Smith, A., and Clutter, D. W., “Machine calculation of compressible laminar boundary layers,” *AIAA Journal*, Vol. 3, No. 4, 1965, pp. 639–647.

[20] Gokcen, T., Skokova, K., Balboni, J., Terrazas-Salinas, I., and Bose, D., “Computational analysis of arc-jet wedge calibration tests in IHF 6-inch conical nozzle,” *47th AIAA Aerospace Sciences Meeting including The New Horizons Forum and Aerospace Exposition*, 2009, p. 1348.

[21] Jones, D. A. (1996). *Principles and prevention of corrosion* (2nd ed.). Prentice Hall.

[22] Oberg, Erik, and Franklin D. Jones. *Machinery's Handbook for Machine Shop and Drafting-room: A Reference Book on Machine Design and Shop Practice for the Mechanical Engineer, Draftsman, Toolmaker and Machinist*. Industrial press, 2016.

[23] Viganò, D., Raybon, I., and Maddalena, L., “Ceramic Insulated Slug Calorimeter for High Enthalpy Flows,” *23rd AIAA International Space Planes and Hypersonic Systems and Technologies Conference*, 2020, p. 2455.

[24] SAAMI, “Voluntary Industry Performance Standards for Pressure and Velocity of shotshell Ammunition for the Use of Commercial Manufacturers,” SAAMI Standard Z299.2 – 2015, 2019

Biographical Information

Blake A. Hamilton was born in March 1989 in Plano, Texas. He enlisted in the United States Marine Corps in 2007. He was stationed at Marine Corps Base Hawaii in 1st Battalion 12th Marine Regiment and served in Iraq in 2008 and 2009. In 2011 he left the Marine Corps and returned to Texas. He briefly attended Texas State University before transferring to the University of Texas at Austin where he completed his Bachelor of Science in Mechanical Engineering in 2016. After professional experience at the Applied Research Laboratories at UT Austin and at Mensor LP, he enrolled at the University of Texas at Arlington for a Master of Science in Aerospace Engineering in 2019. He plans to continue his career as an engineer in the space industry.